Activation of Temoporfin Using Upconverting $LiYF_4$: Tm^{3+}/Yb^{3+} Nanoparticles

Qing Yu

A Thesis

in

The Department

of

Chemistry and Biochemistry

Presented in Partial Fulfillment of the Requirements

for the Degree of Master of Science (Chemistry) at

Concordia University

Montreal, Quebec, Canada

July, 2014

CONCORDIA UNIVERSITY

School of Graduate Studies

This is to certify that the thesis prepared

By: **Qing Yu**

Entitled: **Activation of Temoporfin Using Upconverting $LiYF_4:Tm^{3+}/Yb^{3+}$ Nanoparticles**

and submitted in partial fulfillment of the requirements for the degree of

Master of Science (Chemistry)

complies with the regulations of this University and meets the accepted standards with respect to originality and quality.

Signed by the final examining committee:

_____ Chair
Dr. Gilles Peslherbe

_____ Examiner
Dr. Peter Bird

_____ Examiner
Dr. Pat Forgione

_____ Thesis Supervisor
Dr. John A. Capobianco

Approved by _____
Chair of Department or Graduate Program Director

_____
Dean of Faculty

Date August 14, 2014

ABSTRACT

Activation of Temoporfin Using Upconverting $LiYF_4$: Tm^{3+}/Yb^{3+} Nanoparticles

Qing Yu, MSc.

Concordia University, 2014

A novel and facile approach has been developed to functionalize lithium yttrium fluoride ($LiYF_4$:Tm^{3+}/Yb^{3+}) upconverting nanoparticles with the second generation photosensitizer 5,10,15,20-tetra(m-hydroxyphenyl)chlorin (m-THPC, Temoporfin, Foscan®) for photodynamic therapy. The synthesized nanoconstruct was capable of generating singlet oxygen under near-infrared excitation.

The upconverting nanoparticles $LiYF_4$:Tm^{3+}/Yb^{3+} were prepared *via* the thermal decomposition method. A post-synthesis treatment with HCl was applied to render the nanoparticles monodispersible in aqueous solution, as well as leaving positive charges on the nanoparticle's surface for conjugating potential ligands with negative charges *via* electrostatic interaction.

m-THPC has been modified using a bio-compatible linker 4-(bromomethyl)benzoic acid (BMBA), which not only facilitated the grafting of the m-THPC onto the nanoparticle's surface but also induced a bathochromic shift of the most intense blue absorption peak (Soret band) of m-THPC which resulted in an overlap with the blue emission peak(s) from $LiYF_4$:Tm^{3+}/Yb^{3+}. The overlap is of paramount importance for the fluorescence resonance energy transfer from the nanoparticle to the photosensitizer. The

bathochromic shift of the Soret band has been studied using computational chemistry by stimulating the electronic and optical properties of m-THPC and m-THPC-MBA.

In vitro cell viability test was carried out and the results showed the nanoconstruct was capable of causing cell death up to 70% under 980 nm irradiation for a period of 1 hour. The irradiation with near-infrared light gives a deep tissue penetration and the approach to synthesize this nanoconstruct is very general and could be applied to prepare other photosensitizers in photodynamic therapy.

ACKNOWLEDGEMENTS

I would like to acknowledge and express my heartfelt gratitude to my supervisor Dr. John A. Capobianco for providing me this great research opportunity to work in his lab over the past four years. This project would not be complete without his encouragement and guidance.

I wish to thank my thesis committee members, Prof. Peter Bird and Prof. Pat Forgione for their helpful suggestions towards this project and support throughout the years.

I would like to sincerely extend my appreciation to all my lab colleagues (past and present) of the Lanthanide Research Group, especially Dr. Rafik Naccache, Dr. Nicoleta Bogdan, and Dr. Emma Martin Rodriguez, who continued offering me their great guidance and tons of amazing ideas over the course of my degree. Thanks to their patience and generous help I was able to gain more confidence and experience in doing research and without that I could not have completed this project.

To my dear friends and colleagues Diana Consuelo Rodriguez Burbano, Qianying Li, and Paola Andrea Rojas Gutierrez, we have spent so much great time together and shared so many great memories. I am really grateful to work with you and have you around during the past years.

Above all, I sincerely thank my mom and dad. I know I am very difficult sometimes but you are always so patient with me and giving me continual support and encouragement throughout these years. Thank you for your unconditional love and without you I cannot be the person I am today.

Table of Contents

List of Figures

List of Tables

List of Abbreviations

B3LYP	Becke Three-parameter (exchange), Lee, Yang and Parr (correlation)
BMBA	4-(Bromomethyl)benzoic acid
CPCM	Conductor-like Polarizable Continuum Model
DPBF	1, 3-Diphenylisobenzofuran
ESA	Excited State Absorption
ETU	Energy Transfer Upconversion
FRET	Fluorescence Resonance Energy Transfer
FT-IR	Fourier Transform Infrared
HF	Hartree – Fock
HOMO	Highest Occupied Molecular Orbital
HpD	Hematoporphyrin Derivative
Ln	Lanthanide
Ln^{3+}	Trivalent Lanthanide Ions
LUMO	Lowest Unoccupied Molecular Orbital
MBA	Methyl benzoic acid
MS	Mass Spectrometry
m-THPC	5,10,15,20-Tetra(m-hydroxyphenyl)chlorin
m-THPP	5,10,15,20-Tetra(m-hydroxyphenyl)porphyrin
NIR	Near Infrared
PDT	Photodynamic Therapy
PS	Photosensitizer
QDs	Quantum Dots
STO	Slater Type Orbital
TD-DFT	Time Dependent – Density Functional Theory
TEM	Transmission Electron Microscopy
THF	Tetrahydrofuran
UCNP	Upconverting Nanoparticles
UV	Ultraviolet
XRD	X-Ray Diffraction

Chapter One – Introduction

1.1 Photodynamic Therapy

Photodynamic therapy (PDT) is a treatment for cancer and other malignant disorders that has been intensively developed in recent decades. In photodynamic therapy, the destruction of a target tissue (localized tumor) involves the combination of light of a specific wavelength, oxygen and a photosensitizer (PS) [1-3]. Individually, these three components are harmless however when combined, the putative cytotoxic agent, singlet oxygen ($^1O_2$) is generated to induce cytotoxic reactions in the cells *via* apoptosis or necrosis, leading to the self-destruction of tumor cells. Photodynamic therapy is a stepwise treatment (Figure 1.1) that starts with the injection of the photosensitizer into the bloodstream and requires 1 to 3 days for the tumor cells to absorb the drug. Light exposure is then applied only to the tumor tissues to activate the photosensitizer, which results in the conversion of molecular oxygen to singlet oxygen that induces cell death and destroys the tumor tissues.

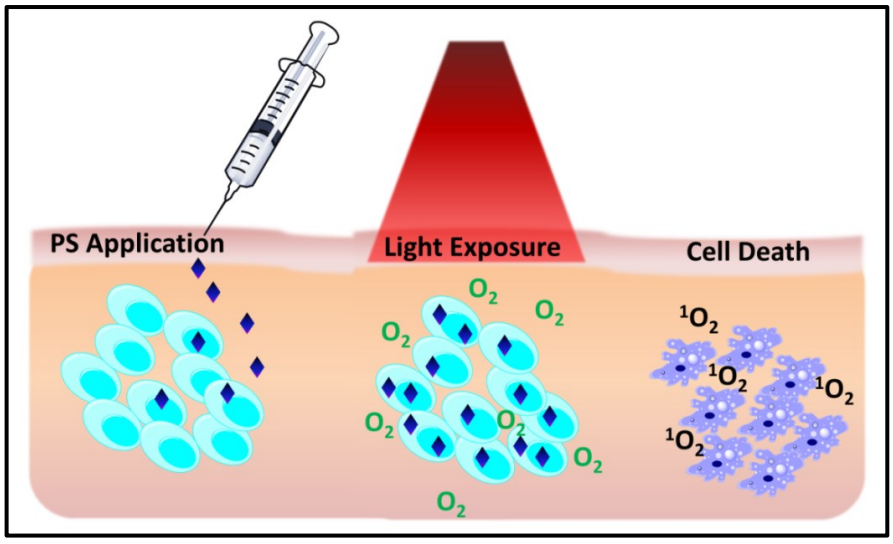

Figure 1.1. Stepwise photodynamic therapy treatment for tumor tissues.

1.1.1 Photosensitizer

Being the key component for photodynamic therapy, a number of photosensitizers have been developed over the years and can be divided into three generations. The first generation photosensitizer is the hematoporphyrin derivative (HpD) that was first approved in 1993 as Photofrin® in Canada for treatments of bladder cancer, lung cancer and esophageal cancer [4]. The second generation PS was developed with higher chemical purity and more defined content such as 5,10,15,20-tetra(m-hydroxyphenyl)chlorin (m-THPC) with trade name Foscan® and generic name Temoporfin [5-7]. It was approved by the European Union in 2001 for the treatment of advanced head and neck cancer. The third generation photosensitizers with higher selectivity towards the target tumor tissues are currently under development [8].

In 1989 *Bonnett et al.* established the requirements for an ideal photosensitizer, which includes lack of dark toxicity, uniform stable composition with high chemical purity, high selectivity towards tumor tissues over healthy cells, a triplet state energy greater than 94 kJ/mol with high singlet oxygen quantum yield, and the ability to absorb red light (above 650 nm) [9]. As a second generation photosensitizer, m-THPC was developed to meet the above requirements and was used to carry out all the work presented in this thesis. The structure of m-THPC is shown in Figure 1.2. m-THPC is derived from the meso-tetra(hydroxyphenyl)porphyrins (m-THPP) *via* a "diimide reduction" [10, 11] which produces a saturated bond between C17 and C18 (Figure 1.2) The introduction of this single bond significantly affects the absorption properties of m-THPC. The absorption band which is used in PDT not only showed a redshift from 644

nm to 650 nm but more significantly a higher molar extinction coefficient of $2.9x10^4$ $M^{-1}cm^{-1}$ compared to m-THPP ($3.4x10^3$ $M^{-1}cm^{-1}$) [12].

Figure 1.2. Chemical structure of the 5,10,15,20-tetra(m-hydroxyphenyl)chlorin (m-THPC) and 5,10,15,20-tetra(m-hydroxyphenyl)porphyrin (m-THPP).

With the improved absorption properties and a 100 to 200 times more potent effect than the first generation photosensitizers, m-THPC quickly became a favorite PDT agent [6]. m-THPC is a porphyrin derivative, with a characteristic UV/Vis spectrum that contains an intense Soret band in the 380 to 500 nm range and a group of weaker bands, Q-bands, in the region 500 to 750 nm. Up to now, photodynamic therapy has made use of red light (Q-bands) to excite the photosensitizer and generate singlet oxygen. However, the Soret band with a significantly higher molar extinction coefficient, 10^5 $M^{-1}cm^{-1}$, has never been used since light in this region has low tissue penetration depth.

1.1.2 Light in Photodynamic Therapy

In addition to the photosensitizer, the excitation light is of paramount importance since the efficiency of photodynamic therapy strongly depends on the excitation wavelength. As previously mentioned, porphyrin-type photosensitizers such as m-THPC have two principal absorption, the Soret band and Q-bands. Excitation with light from either of these bands will provide sufficient energy to activate the photosensitizer. However, porphyrin-type photosensitizers currently use red light in the Q-band region thus not taking advantage of the biological optical window (700 to 1000 nm) where the major biological components such as water (black line), hemoglobin (blue line), and oxyhemoglobin (red line) show their lowest absorption (Figure 1.3).

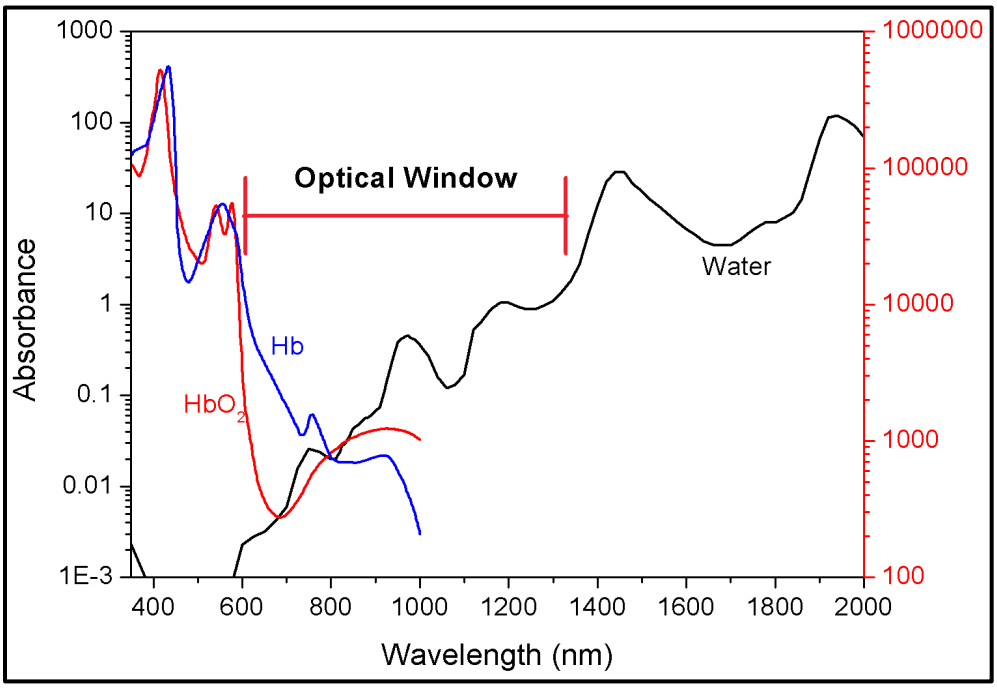

Figure 1.3. Biological optical window [13, 14].

The ideal excitation light for efficient photodynamic therapy should be at a wavelength that not only activates the photosensitizer but also has deep tissue penetration

depth. The Soret band corresponds to the blue region of the spectrum (400 nm) and can only penetrate 1 mm into the biological tissue which limits its applications [15]. As the wavelength increases to 630 nm, which is the excitation currently used in PDT, the penetration depth increases to 10 mm and at a wavelength of 980 nm in the NIR region, the tissue penetration depth is approximately 32 mm (Figure 1.4) which would not limit m-THPC to the treatment of only head and neck cancer. It should be noted that the scattering of light varies as $1/\lambda^4$ [16].

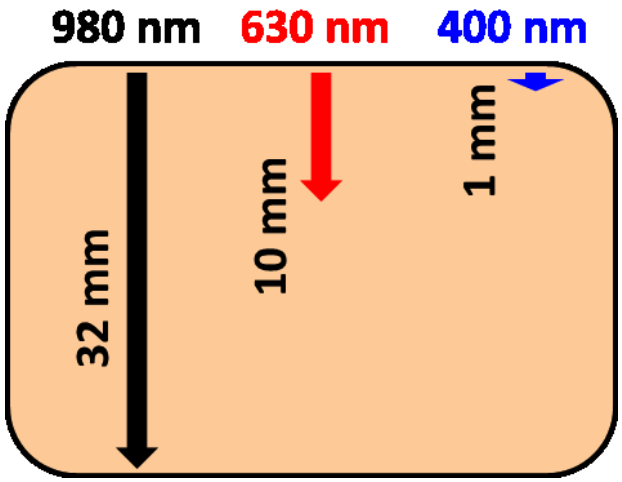

Figure 1.4. Tissue penetration depth of light of different wavelengths: 980 nm, 630 nm, and 400 nm.

Deep tissue penetration can be obtained by making use of the optimal spectral biological window. Unfortunately, photons in this region are energetically too low for $^1O_2$ generation, whereas, direct excitation with high-energy blue light limits the use in biological applications due to its low tissue penetration depth.

1.2 Lanthanide-doped Upconverting Nanoparticles in Biomedical Applications

Lanthanide-doped upconverting nanoparticles (Ln-UCNPs) have emerged as a novel class of luminescent probes with applications in many fields such as bio-imaging, diagnosis, drug delivery, and therapeutics due to the unique optical property of lanthanides known as upconversion [17]. These upconverting nanoparticles can emit UV, visible and/or NIR light upon NIR excitation, typically 980 nm, *via* a multiphoton absorption process.

Lanthanide doped upconverting nanoparticles can be prepared following different synthetic routes to achieve high dispersibility in physiological environments with tunable sizes and emission profiles. The Ln-UCNPs exhibit low cytotoxicity, no photobleaching and low autofluorescence, which makes their use advantageous over quantum dots and organic fluorophores [18]. The Ln-UCNPs have also been proposed as a source of energy for exciting photosensitizers for applications in photodynamic therapy allowing simultaneous targeting and imaging of specific tumor cells [19-24].

1.3 Statement of the Problem

The development of nanotechnology for biomedical applications is extremely important in the field of disease research especially those related to cancer therapy. Photodynamic therapy is one of the most popular therapeutic methods used in cancer treatment and has drawn a great amount of attention in recent years. The essential element in the development of PDT is the PS. Over the past decades, considerable efforts have been undertaken for the development of new PS, which show increased absorption

further in the red (beyond the standard PS absorption of $\lambda_{max} < 650$ nm) enabling the use of light with lower degree of scattering and penetrating deep into the tissues.

The second generation PS, 5, 10, 15, 20-tetra(m-hydroxyphenyl)chlorin (m-THPC, Foscan®), with enhanced absorption of light in the red ($\lambda_{max} = 652$ nm) has been found to be more specific than conventional porphyrins where skin photosensitization, usually a side effect, has been reported to be shorter. However, m-THPC does not make use of the optimal spectral biological window for tissue penetration in the 700 nm to 1μm range. Unfortunately, photons in this region are energetically too low for $^1O_2$ generation. In addition to the band at 652 nm, which has a high molar extinction coefficient ($\varepsilon = 2.9\times10^4$ $cm^{-1}M^{-1}$), m-THPC has another absorption band in the blue region centered at 417nm with a much higher molar absorption coefficient ($\varepsilon = 2.3\times10^5 cm^{-1}M^{-1}$). Excitation of m-THPC at this wavelength would eliminate the problem of low photon energy, however direct excitation with high-energy blue light limits the use in biological applications due to its low tissue penetration depth.

Our group has recently synthesized Tm^{3+}/Yb^{3+}-doped $LiYF_4$ UCNPs via the thermal decomposition method, which showed stronger UV/blue emission following NIR excitation with 980 nm light compared to $NaYF_4$ [25]. Taking advantage of the high penetration depth and minimal autofluorescence of the NIR excitation light, these Ln^{3+}-UCNPs could be used as UV/blue excitation sources in biological applications. Incorporating m-THCP with Ln^{3+}-UCNPs could achieve the excitation of m-THPC upon NIR excitation through a fluorescence resonance energy transfer (FRET) process.

In this thesis we report on the functionalization of $LiYF_4:Tm^{3+}/Yb^{3+}$ UCNPs with m-THPC to demonstrate the generation of singlet oxygen by this molecule using the blue

light obtained following NIR excitation of the nanoparticles. We show that in order to achieve the generation of singlet oxygen from the upconverted blue light emission of the Ln^{3+}-UCNPs, it was necessary to modify the m-THPC using 4-(bromomethyl)benzoic acid (BMBA), which not only facilitated grafting of m-THCP onto the Ln^{3+}-UCNPs but also induced a bathochromic shift of the blue absorption peak.

In addition, establishing the number of methyl benzoic acid (MBA) molecules and their position(s) bonding to the m-THPC is essential since it will shed light on understanding the role, which the MBA molecules have on the spectroscopic properties of m-THPC. Thus, to understand the effects of the substituent and its position) we undertook a computational study using the Gaussian 09 program. Time-dependent density functional theory was combined with Becke Three Parameter Hybrid Functionals (B3LYP) and the basis set 6-31G(d,p) was used to optimize the ground state geometry of the m-THPC and m-THPC-MBA. Gouterman's four orbital model was applied to calculate the absorption of m-THPC and of the m-THPC-MBA.

In vitro cell viability tests were performed to confirm the effect of the nanoconstruct on the cells in the absence and presence of irradiation at 980 nm. HeLa carcinoma cells were incubated for 4 hours with the nanoconstruct (m-THPC-MBA(III)-$LiYF_4$:Tm^{3+}/Yb^{3+}-UCNPs) at concentrations of 0.004 to 0.1 mg/mL in PBS. Cell viability was assayed using the MTT assay, a method based on the activity of mitochondrial dehydrogenase [26].

Chapter Two - Theory

2.1 Photodynamic Therapy

2.1.1 Historical and Clinical Applications of PDT in Cancer Treatment

The application of photodynamic therapy used to treat human diseases dates back 3000 years by the Egyptians, the Chinese and the Indians [27]. The first "modern" application of photodynamic therapy was by Danish scientist Niels Rydberg Finsen, who was awarded the Nobel Prize in Physiology-Medicine in 1903 [28]. The Nobel Committee stated "*in recognition of his contribution to the treatment of diseases, especially lupus vulgaris, with concentrated light radiation, whereby he has opened a new avenue for medical science*". A German student Oscar Raab working under the direction of von Tappeiner contributed to the early development of PDT by reporting on the rapid killing of paramecia by acridine or eosin but only in the presence of light and oxygen. In 1903, von Tappeiner and Jesionek published the first paper reporting on the clinical trial of PDT on patients with skin carcinoma using eosin as the photosensitizer. Other trials on patients by Dreyer and Neisser were terminated due to the severe side effects. In 1911 the use of hematoporphyrin (Hp) in mice was conducted by Walter Hausmann, with some success and the first injection of Hp in humans was in 1913 by Meyer-Betz who injected himself with the photosensitizer. It is reported that he was photosensitive for more than two months which showed the accumulation and retention of Hp in humans [29].

Further studies on the clinical applications of PDT resumed some 70 years later by Dougherty and co-workers. They made significant contributions in the study of a group

of photosensitizers named hematoporphyrin derivatives (HpD), and they reported the first case of successful treatment of tumors in experimental animals using PDT [30, 31]. The investigation on HpD by Dougherty and his co-workers started the modern development of clinical photodynamic therapy.

2.1.2 Role of Singlet Oxygen in PDT

Molecular oxygen has two low-lying singlet excited states $^1\Delta_g$ and $^1\sum_g^+$, 94 (22.5 kcal mol^{-1}) and 158 kJ mol^{-1} (31.5 kcal mol^{-1}) above the triplet state respectively [32]. The electronic configuration of these states differ only by occupancy of the π-antibonding orbitals (Figure 2.1). The triplet ground state ($^3\sum_g^-$) electronic configuration is identical to $^1\sum_g^+$ of the second excited state except that the last two electrons have parallel spins.

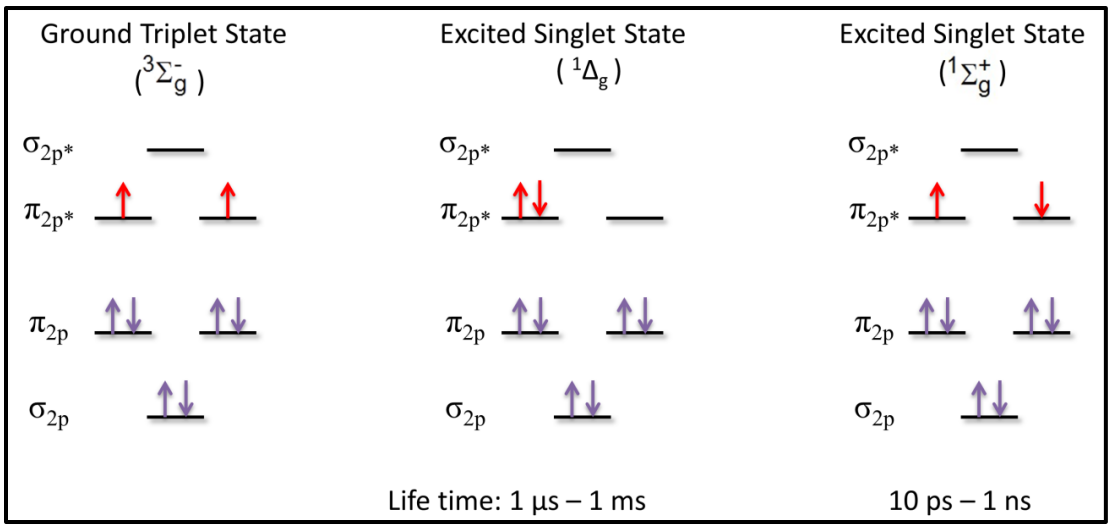

Figure 2.1. Occupation of molecular orbitals in oxygen.

The transition from the $^1\Delta_g$ state to the $^3\sum_g^-$ state is spin forbidden therefore the $^1\Delta_g$ O_2 is a relatively long lived species. The second excited state ($^1\sum_g^+$) of oxygen is short lived since the transition to the $^1\Delta_g$ is spin allowed. The difference in stability of the two

states is confirmed by the radiative lifetimes that have been reported for O_2 ($^1\Delta_g$) and O_2 ($^1\sum_g^+$) which are 64 min and 10 s in the gas phase respectively [33]. The two excited singlet states also have very different lifetimes depending on the nature of the solvent where the lifetime of $^1\Delta_g$ state can vary from 1μs to 1 ms and for the higher energy state 10 ps to 1 ns [34].

2.1.3 Mechanism of Type I and Type II Photosensitization

There are many known sources of singlet oxygen, however we will focus on the photosensitized method of generation since this is the process, which is used in this thesis.

Photosensitized generation of singlet oxygen is a simple process requiring oxygen, light of appropriate wavelength and an appropriate photosensitizer (PS) capable of absorbing and using the energy to excite oxygen to its singlet state. Briefly, upon illumination the photosensitizer is excited, from the ground state S_0 to a short lived excited singlet state S_n. Non-radiative relaxation (Internal Conversion) of S_n to the lowest excited singlet state, S_1, is followed by conversion to the triplet state (T_1) *via* intersystem crossing (ISC) (Figure 2.2). The triplet state has a long lifetime generally in the μs to ms range, which enables the excited photosensitizer to react with the surrounding molecules. The excited triplet state of the photosensitizer may lose its energy either *via* radiative triplet-singlet emission (phosphorescence) or *via* quenching of the excited triplet state that has been shown to be the process which generates the cytotoxic agents needed to induce cell death. This quenching mechanism can occur *via* a Type I or Type II mechanism (Figure 2.3) and both reactions will produce oxidized products [35].

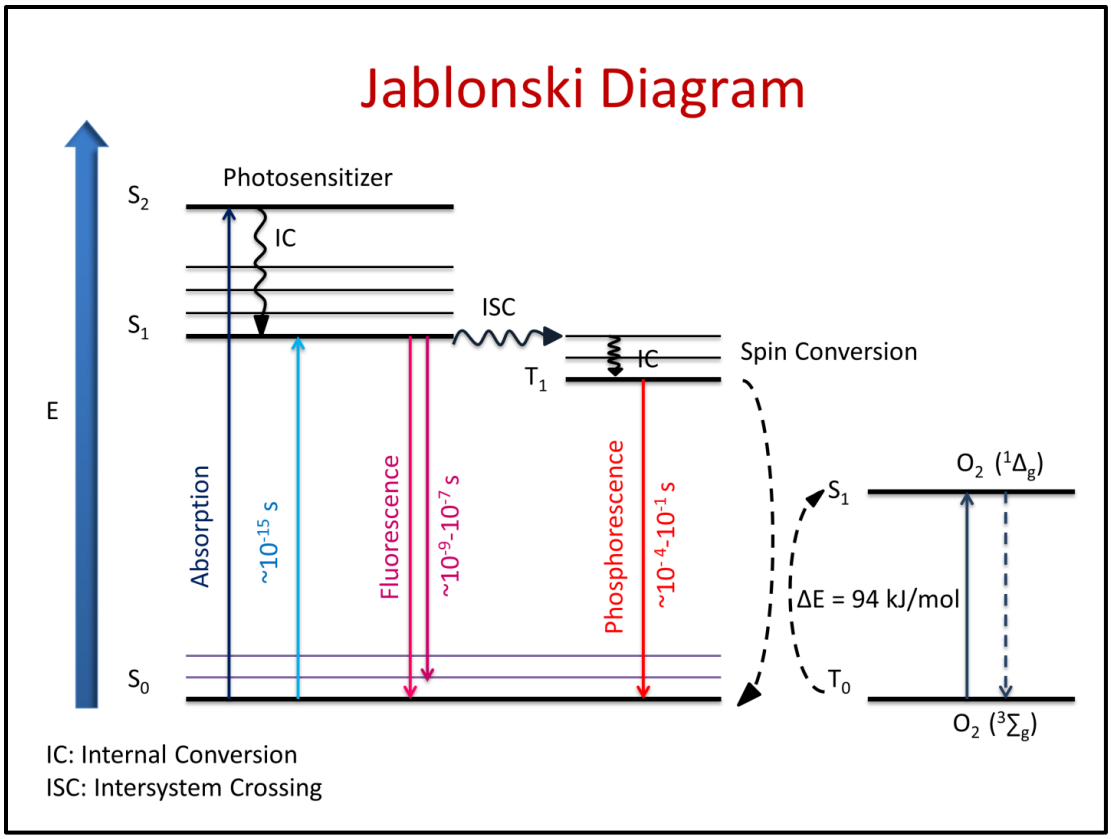

Figure 2.2. Jablonski diagram for the activation of photosensitizer and generation of singlet oxygen.

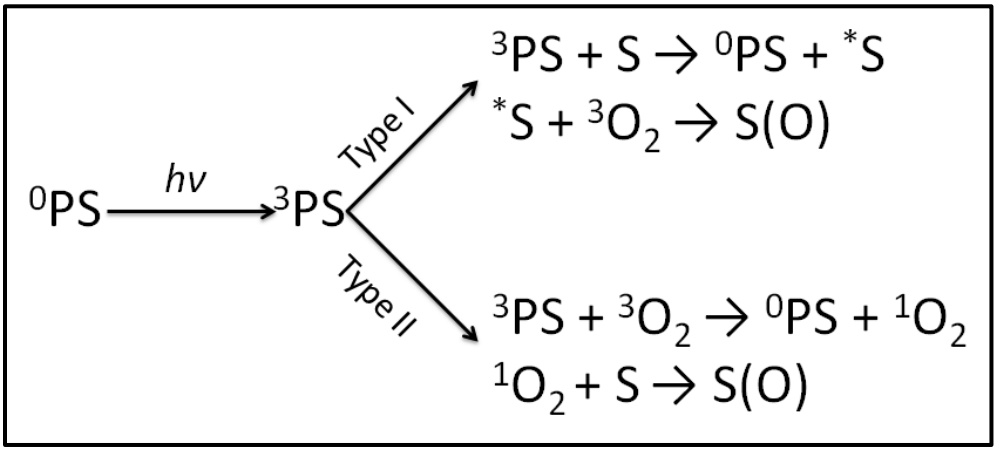

Figure 2.3. Mechanisms of Type I and Type II photosensitization.

As shown in equations 1 to 10 a Type I mechanism occurs *via* hydrogen atom extraction or electron transfer reactions between the photosensitizer's excited state (^{3}PS) and a substrate (S), biological or solvent, to produce radicals and radical ions [36]. It is well known that radical species are very reactive and can react with molecular oxygen to produce reactive oxygen species such as superoxide anion, which lead to the cytotoxic effects. It is worth noting that hydrogen peroxide is a moderate oxidant, however when accumulated it can react with superoxide radicals to produce the hydroxyl radical ($HO^{\bullet-}$) and induce various reactions that lead to the cell deaths.

$$^3PSH + S \rightarrow PS^{\bullet} + SH^{\bullet} \quad (1)$$

$$PS^{\bullet} + O_2 \rightarrow PS + O_2^{\bullet} \quad (2)$$

or

$$^3PS + SH \rightarrow PSH^{\bullet} + S^{\bullet} \quad (3)$$

$$S^{\bullet} + O_2 \rightarrow S + O_2^{\bullet} \quad (4)$$

$$^3PS + S \rightarrow PS^{\bullet-} + S^{\bullet+} \quad (5)$$

$$PS^{\bullet-} + O_2 \rightarrow PS + O_2^{\bullet-} \quad (6)$$

or

$$^3PS + S \rightarrow PS^{\bullet+} + S^{\bullet-} \quad (7)$$

$$S^{\bullet-} + O_2 \rightarrow S + O_2^{\bullet-} \quad (8)$$

The mechanism for Type I reaction starts with the excitation of the ground state photosensitizer ^{0}PS to its triplet state ^{3}PS. As a direct reaction, the excited ^{3}PS reacts with substrate (S) immediately to form neutral radicals (Eq 1 and 3) or radical ions (Eq 5 and 7). In presence of molecular oxygen, the resulting radicals undergo reaction with oxygen to produce superoxide radicals or radical ions (Eq 2, 4, 6, and 8), and the very active peroxide radicals will then convert to hydrogen peroxide *via* spontaneous dismutation (Eq 9) or one-electron reduction (Eq 10).

$$O_2^{\bullet-} + O_2^{\bullet-} + 2H^+ \rightarrow O_2 + H_2O_2 \qquad (9)$$

$$O_2^{\bullet-} + 2H^+ + e^- \rightarrow H_2O_2 \qquad (10)$$

In contrast to a Type I mechanism, in a Type II mechanism ^{3}PS reacts first with molecular oxygen to generate the reactive singlet oxygen that is responsible for the oxidation of the substrate. This mechanism results from an energy transfer between the excited triplet state of the photosensitizer and the ground state of molecular oxygen generating the first excited state of singlet oxygen (Figure 2.2). This mechanism requires the presence of molecular oxygen. The reaction is as follow:

$$\text{Photosensitizer} \rightarrow \text{Photosensitizer*}$$

$$^3\text{Photosensitizer*} + O_2\ (^3\Sigma_g^-) \rightarrow \text{Photosensitizer} + O_2\ (^1\Delta_g)$$

$$O_2\ (^1\Delta_g) + \text{Substrate} \rightarrow \text{Oxidative damage}$$

It is important to note that the Type II mechanism can only occur when the energy gap between the ground state and triplet excited state of the photosensitizer is greater than the energy gap between the ground state and singlet state of oxygen, which is 94 kJ/mol (0.98 eV) [32]. As most of the porphyrin-like molecules have energy gaps greater than 94 kJ/mol and can be used as potential photosensitizers, thus the photosensitization in PDT mostly follows Type II reaction.

2.2 The Lanthanides

The lanthanoids are a group of fourteen elements that follow lanthanum in the periodic table with atomic number from 57 to 71. Lanthanum, which possesses many similar chemical and physical properties to the other members of the group, is included in the lanthanide family although it has been argued that it should not be considered a member since it lacks *f*-orbitals. Also included in this group are the Group III transition metals Y and Sc since they also have many similar properties to the lanthanides. Thus, with the inclusion of scandium and yttrium these elements are known as "rare-earth elements" which is a misnomer since these elements are quite common in the Earth's crust.

Moving along the group corresponds to the successive filling of the 4*f* orbitals from La ($4f^0$) to Lu ($4f^{14}$). Their core electronic configuration is [Xe] $6s^2$ $5d^1$ and a summary of the electronic configurations is shown in Table 2.1. The common oxidation state is +3 however some of the lanthanides may exist as +2 and +4. The trivalent lanthanide ions (Ln^{3+}) have an electronic configuration [Xe]$4f^n$, where n goes from 0 for lanthanum to 14 for lutetium. The 4*f* orbitals are well shielded by the $5s^2$ and $5p^6$ orbitals making it difficult to lose a 4*f* electron. As a consequence the +3 oxidation state becomes the most stable form. Since the valence electrons are the same ($4f^n$) for all the Ln^{3+} ions, they all show very similar reactivity and co-ordination behaviour.

Table 2.1 Electronic configurations of the lanthanide atoms and ions in the 3+ oxidation state [37-39].

Atomic Number	Name	Symbol	Electronic Configuration	
			Atom	Ln^{3+}
21	Scandium	Sc	$[Ar]3d^{1}5s^{2}$	[Ar]
39	Yttrium	Y	$[Kr]4d^{1}5s^{2}$	[Kr]
57	Lanthanum	La	$[Xe]6s^{2}4f^{0}5d^{1}$	[Xe]
58	Cerium	Ce	$[Xe]6s^{2}4f^{1}5d^{1}$	$[Xe]4f^{1}$
59	Praseodymium	Pr	$[Xe]6s^{2}4f^{3}$	$[Xe]4f^{2}$
60	Neodymium	Nd	$[Xe]6s^{2}4f^{4}$	$[Xe]4f^{3}$
61	Promethium	Pm	$[Xe]6s^{2}4f^{5}$	$[Xe]4f^{4}$
62	Samarium	Sm	$[Xe]6s^{2}4f^{6}$	$[Xe]4f^{5}$
63	Europium	Eu	$[Xe]6s^{2}4f^{7}$	$[Xe]4f^{6}$
64	Gadolinium	Gd	$[Xe]6s^{2}4f^{7}5d^{1}$	$[Xe]4f^{7}$
65	Terbium	Tb	$[Xe]6s^{2}4f^{9}$	$[Xe]4f^{8}$
66	Dysprosium	Dy	$[Xe]6s^{2}4f^{10}$	$[Xe]4f^{9}$
67	Holmium	Ho	$[Xe]6s^{2}4f^{11}$	$[Xe]4f^{10}$
68	Erbium	Er	$[Xe]6s^{2}4f^{12}$	$[Xe]4f^{11}$
69	Thulium	Tm	$[Xe]6s^{2}4f^{13}$	$[Xe]4f^{12}$
70	Ytterbium	Yb	$[Xe]6s^{2}4f^{14}$	$[Xe]4f^{13}$
71	Lutetium	Lu	$[Xe]6s^{2}4f^{14}5d^{1}$	$[Xe]4f^{14}$

The luminescence of the Ln^{3+} ions arises from transitions within the 4*f* shell and because this shell is shielded by the filled $5s^2$ and $5p^6$ shells, electrons in the 4*f* orbitals have little participation in chemical bonding, and the crystal field has almost no effect on the energy of the levels, that is, the absorption and emission of the ions are only slightly affected by the environment [40]. Two other important effects arising from the shielding are the sharpness of the emission and absorptions lines and the very small Stokes' shift, which is observed when excitation is achieved directly into the 4*f* levels. The forbidden nature of electronic intra-configurational transitions (Laporte's rule) results in weak *f-f* electric dipole transitions while the much less intense magnetic dipole transitions are allowed [41]. Due to j-mixing and the admixture of vibrational states, electric dipole transitions are observed with intensities of the same order of magnitude as the magnetic dipole transitions.

The Russell-Saunders spin-orbit coupling scheme is valid for the lanthanides and the term symbols for the energy levels are derived using this scheme. Dieke and co-workers in 1950's and 1960's carried out detailed experimental work of the lanthanide transition and their work resulted in the tabulation of the energy levels of the trivalent lanthanide ions in $LaCl_3$ [42]. This resulted in the well-known Dieke energy level scheme shown in Figure 2.4.

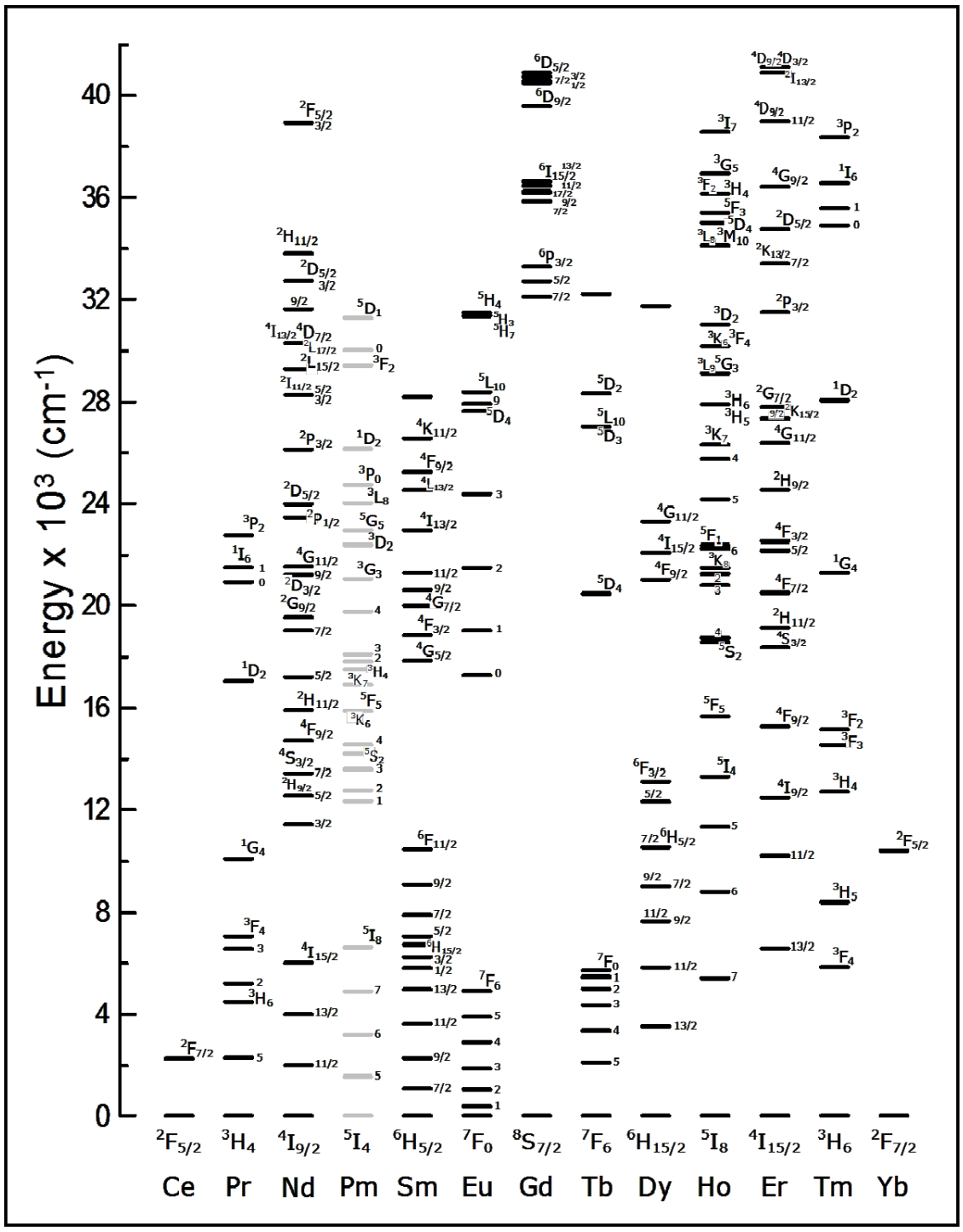

Figure 2.4. The Dieke diagram showing the energy levels of lanthanide ions in $LaCl_3$ [42].

2.3 Upconversion Mechanisms

Upconversion is a process that generates high energy UV and visible light from lower energy radiation such as near infrared or infrared [41, 43-46]. This multiphoton process involves the sequential absorption of two or more photons to populate the luminescent excited state (UV and visible) and it requires a metastable intermediate electronic state with relatively long life time located between the ground state and the luminescent excited state to act as a population reservoir [43]. The ideal candidates to perform efficient upconversion are the trivalent lanthanide in solid-state materials. The trivalent lanthanide ions possess three important characteristics, which makes them ideal candidates for upconversion. Firstly, they have sharp spectroscopic lines with high emission cross sections which result in efficient luminescence. Secondly, the crystal field splitting results in a number of intermediate levels where either energy transfer or excited state absorption can occur. Thirdly, the long intermediate state lifetimes makes these states ideal as population reservoirs from which a second photon can populate the emitting state.

Upconversion occurs *via* three major mechanisms namely excited state absorption (ESA), energy transfer upconversion (ETU) and photon avalanche (PA). The first two mechanisms are related to the work presented in this thesis and will be explained in detail.

2.3.1 Excited State Absorption (ESA) Upconversion

Excited state absorption is the sequential absorption of two photons by a single ion [43, 47] shown in Figure 2.5. Ion X in the ground state (G) absorbs the first photon and

induces the transition to the metastable state E_1 that is intermediate in energy between the ground sate and the fluorescing state E_2. A second photon is absorbed and induces the transition from metastable state E_1 to the upper state E_2 followed by emission and relaxation to the ground state. The energy gaps between ground state G, the intermediate state E_1 and higher excited state E_2 should be close to the pump wavelength.

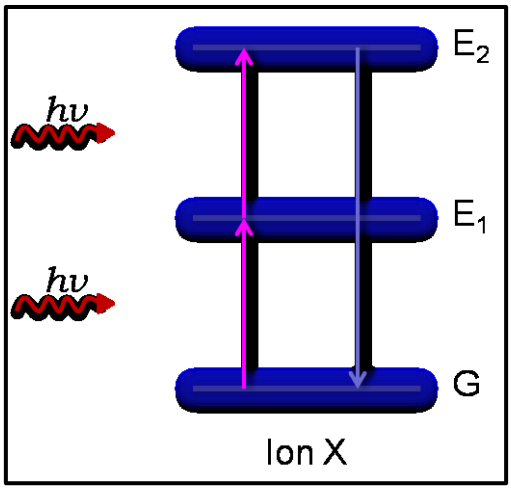

Figure 2.5. Schematic representation of excited state absorption (ESA) upconversion.

2.3.2 Energy Transfer Upconversion (ETU)

Energy transfer upconversion occurs between a pair of neighboring ions *via* the transfer of energy between these ions where one acts as a donor and the other as an acceptor. The mechanism for ETU is shown in Figure 2.6. The first step is the absorption of an incoming pump photon by both donor ions Y, which induces a transition of the donor to the intermediate excited state E_1. The donor ion Y usually has a high absorption cross section. In the second step a non-radiative energy transfer occurs from donor ion Y to the acceptor ion X that promotes ion X to its metastable state E_1, followed by another energy transfer process from the donor ion Y to the acceptor ion X resulting in a

transition to the higher excited state E_2 of the acceptor. The donor ions Y relax to the ground state and the acceptor ions undergo a radiative decay from the excited state E_2 to ground state G. It is very important that the incoming photons have the same energy as the energy gap separating G and E_1 states, and for an efficient ETU the donor and acceptor ions should be in close proximity since energy transfer is dependent on the distance between the neighboring ions. This normally requires a donor ion concentration of 10-50 times that of the acceptor [43-45].

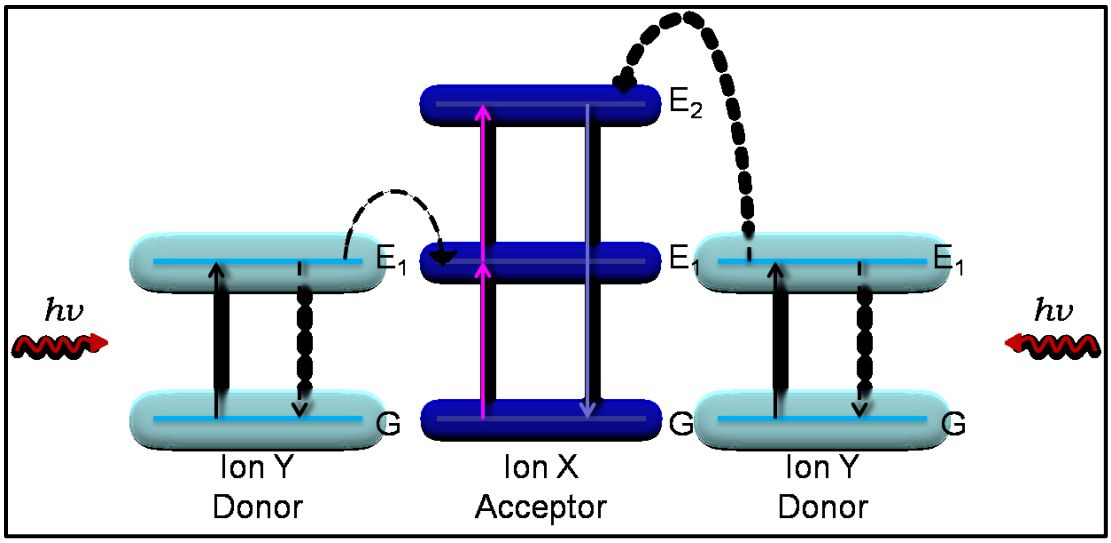

Figure 2.6. Schematic representation of energy transfer upconversion.

2.4 The Fluoride Host

Nanoparticles that exhibit upconversion luminescence have been synthesized using various crystalline host and lanthanide dopants in order to achieve high upconversion efficiency and tunable emission. As mentioned previously, the lanthanide dopants acting as donor-acceptor pairs mainly control the emission profile due to their ladder-like energy levels that facilitate the energy transfer process. The choice of the host material is

extremely important to obtain high upconversion efficiency and high luminescence intensity. Numerous host materials such as oxides, garnets, vanadates, phosphates etc. have been synthesized and studied for potential applications in upconversion. However, fluoride hosts such as $NaYF_4$, $NaGdF_4$, and $LiYF_4$ have been shown to be the ideal hosts for upconversion. Oxides and phosphates have been studied for upconversion however the phonon energies associated with these hosts are relatively high (>500-1000 cm^{-1}) resulting in low upconversion efficiencies due to the enhancement of non-radiative transitions [17]. Phonon energy is the vibrational energy associated with the oscillation of atoms in solids and is non-radiative [48]. The fluoride hosts have been reported to show high upconversion efficiency. This has been attributed to their low phonon energies (~350 cm^{-1}), which renders them ideal hosts for the upconversion process [25].

The excited states of lanthanide ions relax via two competitive pathways namely by light emission and phonon emission processes [49, 50]. The rate of phonon emission, ω, depends on the number of phonons emitted simultaneously to bridge the energy gap and is expressed by equation 11.

$$\omega \ \alpha \ \exp(-k\Delta E/h\upsilon_{max}) \qquad \textbf{(11)}$$

where, ΔE is the energy gap to the nearest lower level and $h\nu_{max}$ is the maximum energy of phonons coupled to the emitting states. The phonon emission rate, ω, decreases rapidly with an increase in ΔE, so that the competitive light emission or radiative process becomes dominant. Thus, the luminescence efficiency of an excited state is based on the energy gap that needs to be bridged to the next lower state. Generally, the larger is the number of phonons needed to convert the excitation energy into phonon energy, the

lower is the efficiency of the non-radiative process. Hence, to enhance the emission efficiency by reducing the non-radiative rate, it is desirable to have the lanthanide ions incorporated into a host of very low frequency phonons. Among investigated hosts, fluoride materials have the lowest phonon cutoff energy and generally exhibit the highest UC efficiency due to the minimization of non-radiative losses in the intermediate states or the emitting states [25].

In addition to the low phonon energy, the local crystal field can also affect the upconversion. The crystal field of a host material has a profound effect of the upconversion efficiency of lanthanide emitters, as the local crystal symmetry surrounding a lanthanide ion strongly influences its optical properties. A less symmetric crystal phase is generally favorable for the upconversion efficiency, as the intermixing of the lanthanide ion's *f* states with higher electronic configurations can be more manifested. For example, hexagonal $NaYF_4$:Er^{3+}/Yb^{3+} microcrystals exhibit visible upconversion luminescence, which is 4.4 times higher than its cubic counterpart [51-53].

2.4.1 The Host $LiYF_4$

An ideal host material should be transparent in the spectral range of interest, have high optical damage threshold, be chemically stable and be associated with high upconversion efficiency. In this thesis $LiYF_4$, was chosen as the host material because it not only shows all of the properties mentioned above but also because it is one of the most efficient host materials for the upconversion process [25]. In contrast to $NaYF_4$ host matrix, $LiYF_4$ not only offers comparable emission intensity but also generates additional strong emission lines in the blue and UV (Figure 2.7).

$LiYF_4$ is one of the best known fluorides that have a tetragonal sheelite structure in reference to $CaWO_4$. Lithium ions are in the center of tetrahedra fluoride ions. Yttrium ions are in the center of polyhedra composed by $8F^-$ (Figure 2.8). Y^{3+} can be substituted by trivalent lanthanide ions such as Er^{3+} and Tm^{3+}. $LiYF_4$ has a high capacity for isomorphous replacement of yttrium ions by trivalent lanthanides without strongly affecting the lattice structure, due to their similar size [54].

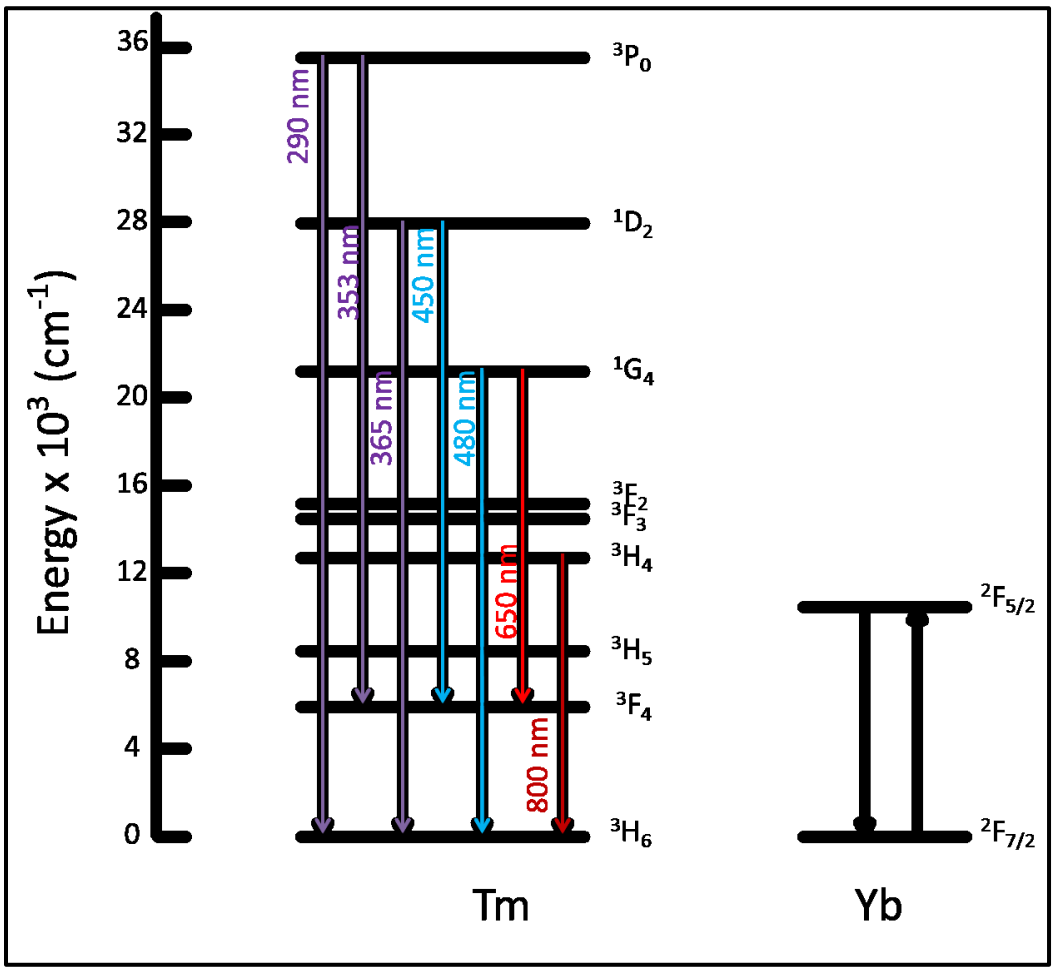

Figure 2.7. Energy levels of Tm^{3+} and Yb^{3+} trivalent ions involved in ETU process. Possible emissions from Tm^{3+} ions are shown in corresponding colors.

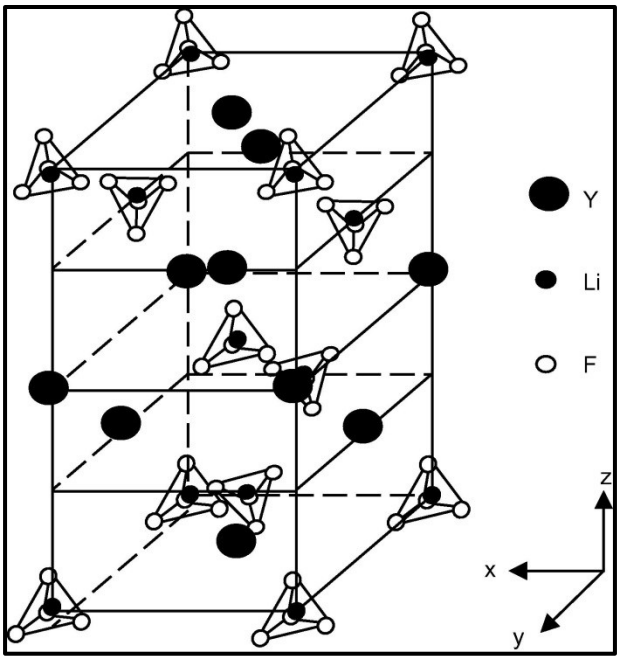

Figure 2.8. Crystal structure of $LiYF_4$ [54].

2.5 Computational Approach to Study the Spectroscopic Properties of the Photosensitizer

Computational chemistry is focused on obtaining results relevant to chemical problems not directly developing new theoretical models. Computational chemistry makes use of the computer as an experimental tool much like for example NMR. Computational chemistry is used to simulate chemical structures, reaction pathways and properties of molecules, which are difficult to examine using traditional experimental approaches. The computational simulation is based on two fundamental methods quantum mechanics (QM) and molecular dynamics (MD) and the former is generally used to study the structure and electronic properties of molecules [55, 56].

2.5.1 Background and Methodology

Quantum mechanics is used in computational chemistry to calculate chemical and physical properties related to electronic distribution based on the time-dependent Schrodinger equation:

$$\left\{\frac{-h^2}{8\pi^2 m}\nabla^2 + V\right\}\Psi(\mathrm{r},\mathrm{t}) = \frac{ih}{2\pi}\frac{\partial\Psi(\mathrm{r},\mathrm{t})}{\partial \mathrm{t}} \qquad (12)$$

where m is the mass of a single particle, Ψ is the wavefunction of the motion of that particle, h is Planck's constant, V is the potential field in which the particle is moving and ∇^2 is the Laplacian operator,

$$\nabla^2 = \frac{\partial^2}{\partial x^2} + \frac{\partial^2}{\partial y^2} + \frac{\partial^2}{\partial z^2} \qquad (13)$$

In computational calculations three main classes of electronic structure methods are used; *semi-empirical, ab initio* and *density functional theory* (DFT) which are all based on the laws of quantum mechanics and use a variety of approximations to obtain the solution to specific problems. *Semi-empirical* methods use experimental parameters to simplify calculations and have been used extensively for organic molecules to obtain qualitative information or for large systems to perform preliminary optimizations prior to the subsequent high level calculations. *Semi-empirical* methods are very efficient methods with good accuracy and low cost, however there are limitations. The experimental parameters for all the atoms in the system studied must be developed due to its "*empirical*" nature. In contrast to *semi-empirical* methods, *ab initio* methods use only the mathematical approximations derived from the laws of quantum mechanics to perform calculations and obtain results with high quality however at a much higher cost (in computer time). To obtain high quality results and decrease the cost, *density*

functional theory methods have been developed in recent years, which have been widely used. The DFT and *ab initio* methods are similar however DFT calculations give significantly higher accuracy due to the inclusion in the calculation of electron correlation effects. When modeling a molecular system the electron correlation effects are taken into consideration using the kinetic energy, the electron-nuclear interaction, and the Coulomb repulsion separately which assumes inter-electronic interaction. This represents the system more accurately than the Hartree-Fock (HF) theory which considers the electron effect as an average. In the DFT methods the electron correlation is computed *via* functionals of electron density and one of the best known is the hybrid exchange-correlation functionals B3LYP (Becke's three-parameter, Lee-Yang-Parr).

The choice of a theoretical method and functionals is the first and the most important step in performing a calculation on the molecular system of interest. Another important component in the calculation is the basis set, a mathematical description of molecular orbitals using linear combinations of functions. The accuracy and cost of a calculation is highly dependent on the choice of basis set. A minimal basis set uses fixed-sized atomic orbitals with minimum number of basis functions and one example is STO-3G used in *ab initio* calculations in which STO stands for the Slater-type orbital and 3G means three Gaussian primitives are included for each basis function. For calculations that require a higher level of accuracy, split valence basis sets are developed in addition to the minimal basis sets and two or more sizes of basis function for each valence orbital are been included to allow orbitals to change size. For example, the set 6-31G, six primitives are used in each core atomic orbital basis function and the valence orbital is described by two basis functions that have three primitive GTOs and one primitive GTO

respectively. In addition to changing orbital size, polarization functions are used to allow orbitals to change shape by adding high angular momentum functions to valence electrons. As an extension to the basis set 6-31G, 6-31G(d) includes d functions for heavy atoms and 6-31G(d,p) includes d functions for heavy atoms plus additional p functions for hydrogen. For systems in which electrons are located far from the nucleus, such as molecules in their excited states, diffuse functions are added to the basis set to allow orbitals to occupy a larger region of space and yield more accurate results. The notation of a basis set with diffuse functions is represented by the "+" sign, 6-31+G(d) indicates a basis set with diffuse function on heavy atoms only and 6-31++G(d) is with diffuse function on both heavy atoms and hydrogen atoms.

2.5.2 Modeling Excited State Using TD-DFT Method

In quantum mechanics excited states of molecular systems are the stable electronic configurations with energies higher than the ground state and are closely related to the electronic transitions and spectroscopic properties. TD-DFT is one of the more commonly used methods in calculating excitation energies for the excited states and has been found to be accurate in simulating absorption spectra of organic molecules such as porphyrin and chlorin [57, 58]. The four-orbital model developed by Gouterman in the 1960s is the mostly used theoretical basis for the prediction of porphyrin UV/Vis absorption spectra [59, 60]. As shown in Figure 2.9 the characteristic Soret bands and Q-bands in a typical porphyrin arise from transitions between HOMO and HOMO -1 π orbitals and LUMO and LUMO +1 π^* orbitals. Several factors such as the conjugation pathway, symmetry and substituent have been shown to affect these orbitals thus leading

to a change in the absorption spectra [59, 61-65]. Therefore in this thesis TD-DFT has been applied to model the excited states of the photosensitizers m-THPC and m-THPC-MBA for the interpretation of UV/Vis absorption spectra and understanding the effect of MBA linker.

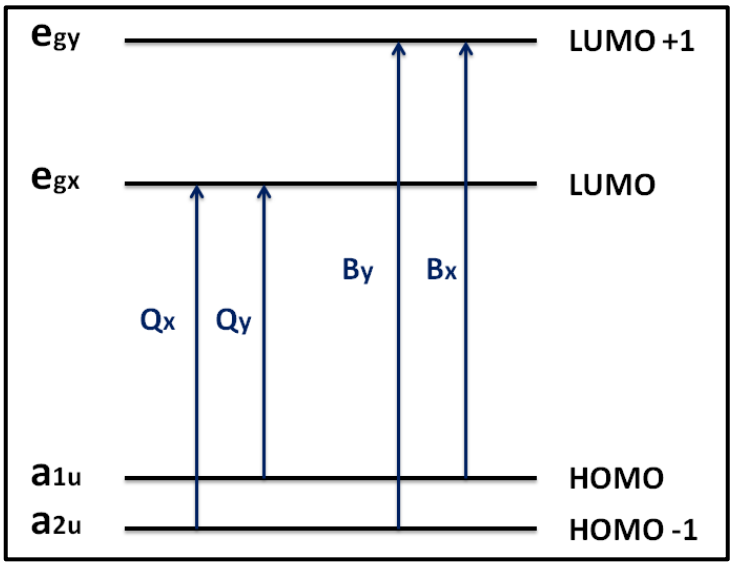

Figure 2.9. Energy levels of the four Gouterman orbitals and transitions that give rise to Q band and Soret (B) bands.

Chapter Three – Experimental and Characterization Techniques

3.1 Thermal Decomposition Synthesis of Lanthanide-doped Nanoparticles

The $LiYF_4:Tm^{3+}$ (0.5%)/Yb^{3+} (25%) upconverting nanoparticles were synthesized *via* the thermal decomposition method established by our group [25]. The two major steps involved in the synthesis are the preparation of the trifluroacetate lanthanide precursors, and the formation of the oleate capped nanoparticles.

3.1.1 Synthesis of Y^{3+}, Tm^{3+}, and Yb^{3+} Trifluroacetate Precursors

The lanthanide trifluoraceate precursors were prepared by dissolving 210.3 mg (0.931 mmol) of Y_2O_3, 123.2 mg (0.313 mmol) of Yb_2O_3 and 2.4 mg (0.00625 mmol) of Tm_2O_3 in a mixture of 5 mL of trifluoroacetic acid (CF_3COOH) and 5 mL of water. The reaction mixture was heated to 80 °C under reflux for 12 hours and then slowly evaporated to dryness at 60 °C.

3.1.2 Synthesis of Oleate-capped $LiYF_4$: Tm^{3+}/Yb^{3+} Nanoparticles

In the second step of the synthesis procedure a solution (solution A) containing 12.5 mL of oleic acid and 12.5 mL of 1-octadecene was degassed at 150 °C for 30 min and then maintained at the same temperature under an argon atmosphere. CF_3COOLi, 299.9 mg (2.5 mmol) was added to the dried lanthanide precursor solids and dissolved in 7.5 mL of oleic acid and 7.5 mL of 1-octadence (solution B). Solution B was degassed at 125 °C under vacuum. Solution A was heated to 315 °C under a gentle flow of argon gas. Solution B was added to solution A using a syringe and pump system at a rate of 1.5

mL/min. The solution was heated under argon at 315 °C for 90 min with continuous stirring. The solution was allowed to cool to room temperature. Nanoparticles were precipitated out using ethanol (99%). The nanoparticles were isolated by centrifugation at 4000 rpm, which is equivalent to relative centrifugal force of 1350g, for 15 min and then washed with ethanol/hexane (4:1) mixture twice to remove any impurities.

3.1.3 Preparation of Water Dispersible Nanoparticles *via* Removal of the Capping Ligand Oleate

The as synthesized $LiYF_4$:Tm^{3+}/Yb^{3+}-UCNPs are hydrophobic due to the hydrophobic capping ligand oleate on their surface. To render the nanoparticles hydrophilic and water dispersible, the capping ligand oleate was removed *via* a simple HCl treatment [66]. An appropriate amount of oleate capped Ln-UCNPs were dispersed in a 0.1 M solution of HCl and maintained at pH at 4 while stirring for 2 hours. During this reaction the carboxylate groups of the oleate ligand were protonated to produce oleic acid. After the reaction was completed the aqueous solution was mixed with diethyl ether to remove the oleic acid. The extraction with diethyl ether was carried out three times. The combined diethyl ether layers were re-extracted with water. The Ln-UCNPs in the water dispersible fraction were recuperated by centrifugation (4000 rpm) after precipitation with acetone. The nanoparticles were finally dispersed in water.

3.2 Modification of Photosensitizer Temoporfin

The photosensitizer m-THPC was modified by adding a biocompatible linker, 4-bromomethyle benzoic acid, in order to add a carboxylate functionality, which allows for the functionalization to the UCNPs as well as cause a red shift of m-THPC's Soret band.

3.2.1 Coupling Reaction between m-THPC and 4-Bromomethyl Benzoic Acid

m-THPC was kindly provided by Biolitec AG in Germany. 4-(Bromomethyl)benzoic acid, 97% purchased from Alfa Aesar was used as a linker to bond m-THPC to the Ln-UCNPs. A sodium hydride suspension in 10 mL of tetrahydrofuran was added to 20 mg (0.029 mmol) of m-THPC. The reaction mixture was heated under reflux for 30 min with stirring. 24.9 mg (0.060 mmol) of 4-(bromomethyl)benzoic acid was added dropwise and the mixture was refluxed for 12 hours. After cooling to room temperature water was added to the mixture and THF was removed under vacuum. The aqueous solution was adjusted to pH = 2 using HCl at 5 °C, and the precipitated 5,10,15-tris(m-hydroxyphenyl)-chlorin-20-methyl benzoic acid (m-THPC-MBA) was recovered.

3.2.2 Conjugation of Photosensitizer to $LiYF_4$: Tm^{3+}/Yb^{3+} Nanoparticles

Typically, 10 mg of oleate-free $LiYF_4$:Tm^{3+}/Yb^{3+}-UCNPs were dispersed in 4 mL of water followed by the addition of 1 mg of m-THPC-MBA in 1 mL of ethanol. The mixture was adjusted to neutral pH to deprotonate the carboxylic group on the m-THPC-MBA and stirred for 6 days at room temperature. The resulting m-THPC-MBA-$LiYF_4$:Tm^{3+}/Yb^{3+}-UCNPs were precipitated in acetone and then isolated by

centrifugation at 4000 rpm for 15 min. The m-THPC-MBA has relatively high solubility in acetone and all the free molecules would be removed with the supernatant.

3.3 Computational Calculations

Calculations of the electronic absorption spectra of m-THPC and m-THPC-MBA were carried out using the Gaussian 09 software package on the Golem Server at Concordia University.

The molecular geometries of the ground singlet state were optimized together with the frequency at the TD-DFT (time-dependent density functional theory) level using Becke's three-parameter functional with the Lee-Yang-Parr correlation functional (B3LYP) with basis set 6-31G(d,p). The solvation model CPCM (conductor-like polarizable continuum model) was applied to stimulate the experimental environment using ethanol as the solvent. The method TD-DFT/B3LYP with basis set 6-31G(d,p) was used to calculate the absorption spectra of the geometry optimized m-THPC and three m-THPC-MBA isomers in liquid phase (CPCM, with ethanol as solvent). The excited state energies of both singlet and triplet states were calculated for 15 transitions.

3.4 Detection of Singlet Oxygen

The singlet oxygen generation of the photosensitizer and the nanoconstruct was measured using the singlet oxygen trap 1, 3-diphenylisobenzofuran (DPBF). The chemical trap DPBF reacts specifically with the singlet oxygen to form an endoperoxide upon a cycloaddition reaction as shown in Scheme 3.1. The DPBF trap is yellow in color and has a characteristic absorption band centered at 415 nm. Upon reaction with singlet

oxygen, a colorless product is formed and the decrease in absorption (415 nm) is used to calculation the amount of singlet oxygen generated [67, 68].

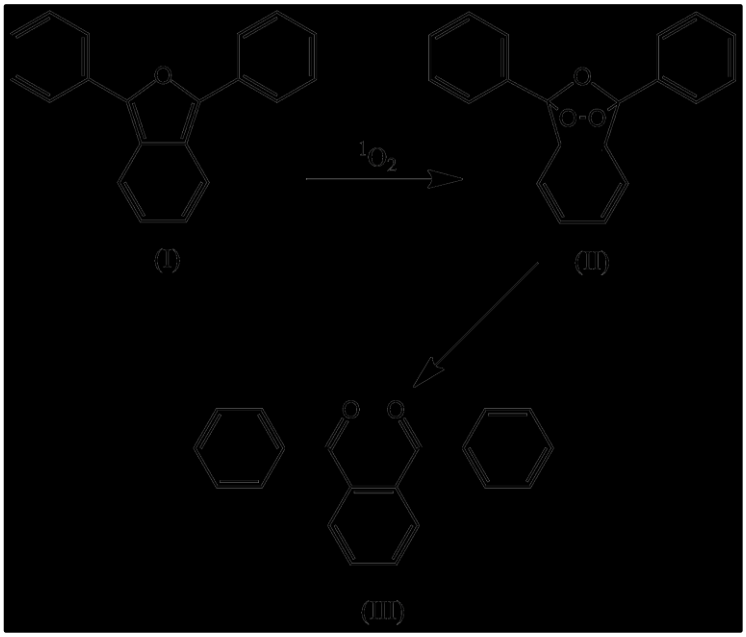

Scheme 3.1. Reaction of chemical trap DPBF (I) and singlet oxygen to form a colorless intermediate endoperoxide (II).

The singlet oxygen generated by the photosensitizer and the nanoconstruct under irradiation using 435 nm and 980 nm light, was monitored using the chemical trap DPBF. All the measurements were performed in air-saturated propylene glycol/ethanol mixture solution in a 10 mm x 10 mm quartz cuvette. The total volume of solution used was 2 mL containing 2.5 x 10^{-5} M of DPBF and 5 x 10^{-5} M of m-THPC-MBA which corresponds to 1 mg/mL of m-THCP-MBA-$LiYF_4$:Tm^{3+}/Yb^{3+}-UCNPs in solution. The samples were kept in dark at all the time except during the irradiation under excitation light.

3.5 *In Vitro* MTT Assay

In vitro viability of HeLa cells exposed to the m-THPC-MBA(III)-$LiYF_4$:Tm^{3+}/Yb^{3+}-UCNPs was analyzed by the MTT (3-[4,5-dimethylthiazol-2-yl]-2,5-diphenyltetrazoliumbromide) colorimetric assay in the absence and presence of irradiation at 980 nm. This method is based on the capacity of the dehydrogenases of living cells to reduce the salt of tretazolio MTT to a colored and insoluble compound, formazan.

In the first experiment HeLa cells were incubated for 4 hours with the m-THPC-MBA(III)-$LiYF_4$:Tm^{3+}/Yb^{3+}-UCNPs followed by the cells being incubated with MTT (0.1 mg/ml in DMEM with 10% SFB and 1% L-glutamine) for 4 hours at 37 °C. The medium with the MTT was removed and the crystallized formazan was suspended with 1 ml of dimethylsulphoxide (DMSO). Immediately after, the absorbance at 540 nm was measured using plate reader (Espectra Fluor 4, Tecan). Cell viability was obtained as a percentage relative (100% viability) to the mean of absorption obtained from the control cells (incubated in the absence of m-THPC-MBA(III)-$LiYF_4$:Tm^{3+}/Yb^{3+}-UCNPs).

In the second experiment the cells were incubated for 4 hours with the m-THPC-MBA(III)-$LiYF_4$:Tm^{3+}/Yb^{3+}-UCNPs, and exposed to NIR radiation during 1 hour (using Hydrosun®750 irradiator with a water filter). Cell viability was also estimated as a percentage relative (100% viability) to the mean of absorption obtained from the control cells (cells incubated without nanoparticles but exposed to NIR radiation for1 hour).

3.6 Characterizations Techniques

3.6.1 Fourier Transform Infrared (FTIR) Spectroscopy

FTIR spectra of the as-synthesized oleate-capped $LiYF_4$:Tm^{3+}/Yb^{3+}-UCNPs, and the oleate-free $LiYF_4$:Tm^{3+}/Yb^{3+}-UCNPs were measured on a Nicolet 6700 FTIR spectrometer by using KBr as the background.

3.6.2 Transmission Electron Microscopy (TEM)

TEM analysis of the colloidal dispersion of $LiYF_4$: Tm^{3+}/Yb^3 -UCNPs was performed using a Philips CM200 microscope operating at 200 kV equipped with a charge-coupled device (CCD) camera (Gatan). Prior to analysis, a sample of the nanoparticles was dispered in toluene to yield a 0.5 wt% solution. A few drops of the resulting solution were evaporated on a formvar/carbon film supported on a 300 mesh copper grid (3 mm in diameter).

3.6.3 X-Ray Powder Diffraction (XRPD)

XRPD patterns were measured using a Scintag XDS-2000 Diffractometer equipped with a Si(Li) Peltier-cooled solid state detector, a Cu Kα source using a generator power of 45 kV and 40 mA, divergent beams (2 mm and 4 mm), and receiving beam slits (0.5 mm and 0.2 mm). The scan range was set from 10-90° 2θ with a step size of 0.02° and a count time of 2 s. The sample was measured using a quartz “zero background” disk.

3.6.4 Upconversion Luminescence Spectroscopy

The upconversion visible emission spectra of the oleate-free $LiYF_4:Tm^{3+}/Yb^{3+}$-UCNPs and the Ln^{3+}-UCNP-m-THCP-MBA were obtained upon 980 nm excitation, using a Coherent 6-pin fiber-coupled F6 series 980 nm laser diode (power of 615 mW), coupled to a 100 μm (core) fiber. For the upconversion studies, the samples (1 wt% in EtOH/propylene glycol) were placed in a Hellma, QS quartz cuvette (1 cm path length). The upconverted visible emissions were collected at right angle with respect to the incident beam and subsequently dispersed by a 1m Jarrell-Ash Czerny-Turner double monochromator with an optical resolution of ~0.15 nm. The emission was detected by a thermoelectrically cooled Hamamatsu R943-02 photomultiplier tube. A preamplifier, model SR440 Standard Research Systems, processed the photomultiplier signals and a gated photon counter model SR400 Standard Research Systems data acquisition system was used as an interface between the computer and the spectroscopic hardware. The signal was recorded under computer control using the Standard Research Systems SR465 software data acquisition/analyzer system.

The UV emissions were collected using a Spex Minimate ¼ m monochromator and detected with an Oriel 70680 photomultiplier tube. It should be noted that while the UV and visible emissions are measured with different detectors, they overlap in the blue region. Thus, by measuring the overlapping regions with both monochromators, under identical conditions, the intensity of the UV emissions could be compared to the visible ones.

3.6.5 UV/Vis Absorption Measurement

UV/Vis absorption spectra of m-THCP, m-THCP-MBA isomers and m-THPC-MBA(III)-$LiYF_4$:Tm^{3+}/Yb^{3+}-UCNPs were all measured in solvent mixture propylene glycol/EtOH and were recorded using Varian (Mulgrave, Victoria, Australia) Cary 5 and 5000 spectrophotometers.

3.6.6 Mass Spectrometry

Mass spectrometry measurements were performed using a LC-MSD TOF (Agilent) using ESI as the ionisation source with mass range of 50 – 8000 m/z.

Preparative Liquid Chromatography – Mass Spectrometry (Prep LC-MS) was used to separate the products and m-THPC, using an MSQ Plus TM Single Quadrupole Mass Spectrometer from Thermo Scientific TM.

Chapter Four - Characterization of $LiYF_4:Tm^{3+}/Yb^{3+}$-UCNPs

The work proposed in this thesis aimed at developing a nanoconstruct using $LiYF_4:Tm^{3+}/Yb^{3+}$ upconverting nanoparticles (UCNPs) and the photosensitizer Temoporfin for photodynamic therapy in "deep" tissue. Our group has recently synthesized $LiYF_4:Tm^{3+}/Yb^{3+}$-UCNPs that showed stronger UV/blue emission following NIR excitation with 980 nm light compared to $NaYF_4$ [25], therefore these UCNPs were used as the platform for the nanoconstructs.

4.1 Morphology and Size

The thermal decomposition synthesis was used to produce the lanthanide-doped nanoparticles upconverting nanoparticles $LiYF_4:Tm^{3+}/Yb^{3+}$ to be used as the excitation source and platform for the photosensitizer. The oleate-capped $LiYF_4:Tm^{3+}/Yb^{3+}$-UCNPs showed a diamond-like morphology with an average size of 86 nm long diagonal length with an aspect ratio of 1.7. The transmission electron microscopy (TEM) results and size distribution are shown in Figure 4.1. The nanoparticles show a narrow particle size distribution.

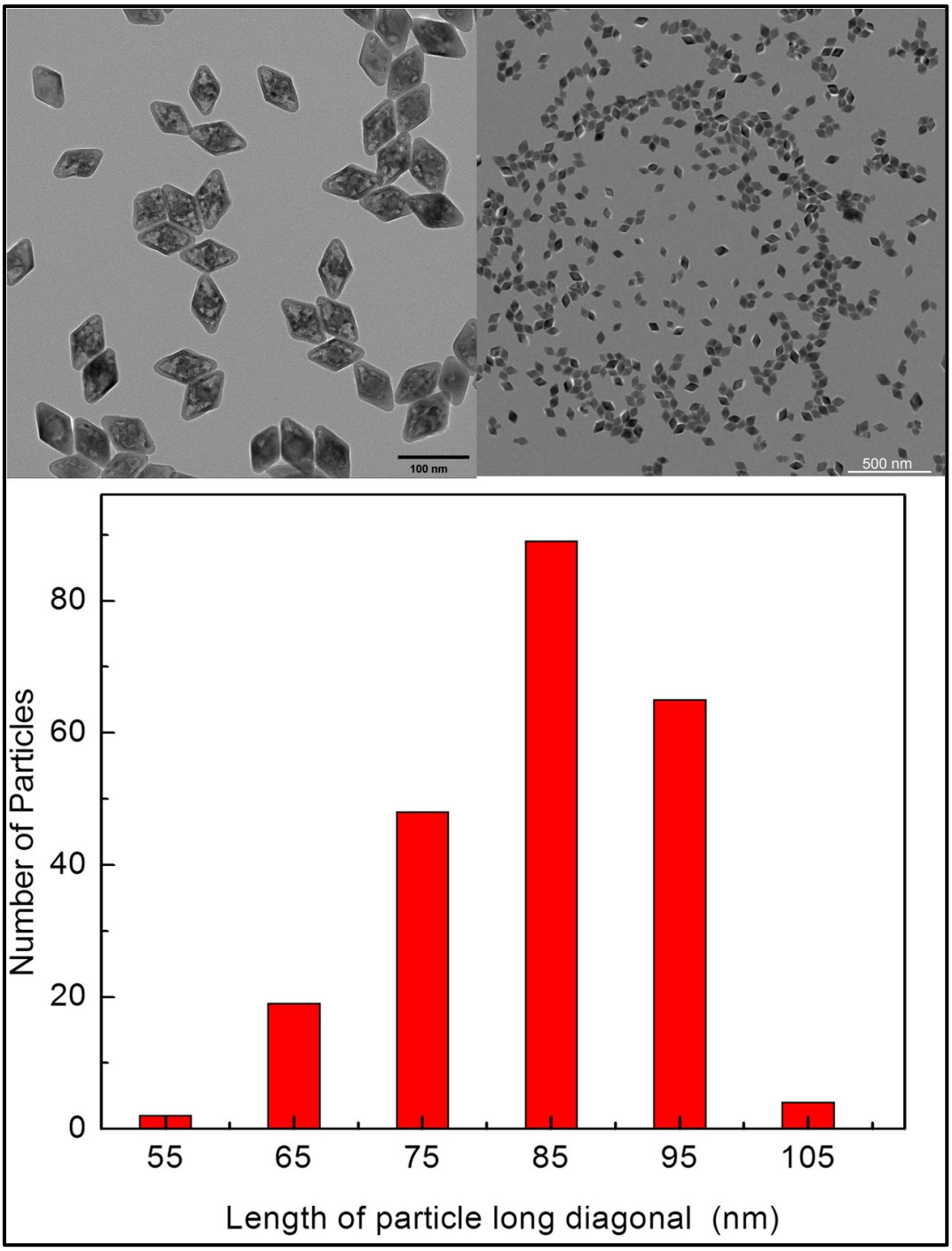

Figure 4.1. TEM image of oleated-capped $LiYF_4$: Tm^{3+}/Yb^{3+}-UCNPs (5 wt% in toluene) and size distribution showing the average length of the particles' long diagonal.

4.2 Crystal Phase

From the high-resolution TEM image, Figure 4.2, the distance between the lattice fringe was measured to be 4.6 Å which corresponds to the d-spacing for the (101) planes in the tetragonal $LiYF_4$ structure.

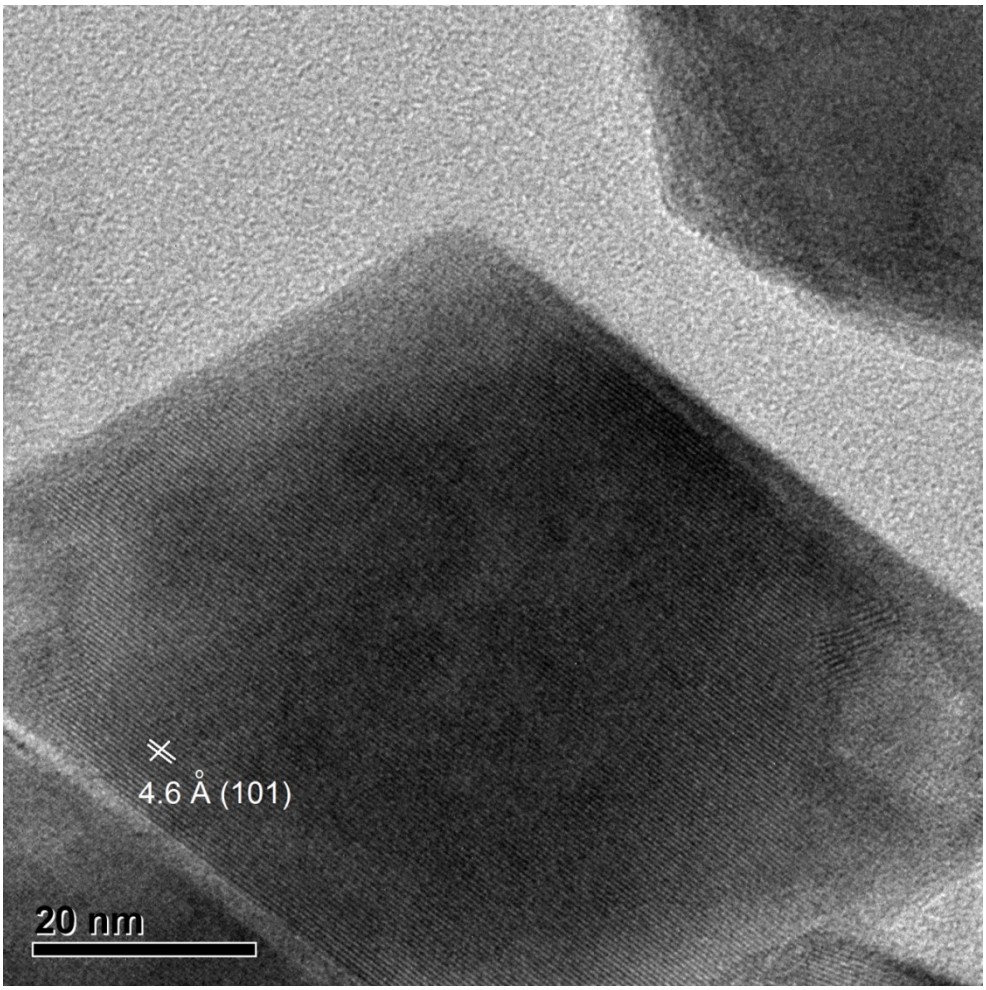

Figure 4.2. High resolution TEM image showing the lattice arrangement of the atoms in the crystals. The distance between the adjacent planes (d-spacing) was measured to be 4.6 Å, which matches the (101) planes in $LiYF_4$.

Figure 4.3 shows the powder X-ray diffraction (XRD) pattern of the $LiYF_4$: Tm^{3+}/Yb^{3+}-UCNPs and the calculated standard JCPDS pattern. The peak positions correspond closely to the reported pattern of tetragonal $LiYF_4$ (JCPDS No. 81-2254). The corresponding *hkl* planes are shown for each peak indexed.

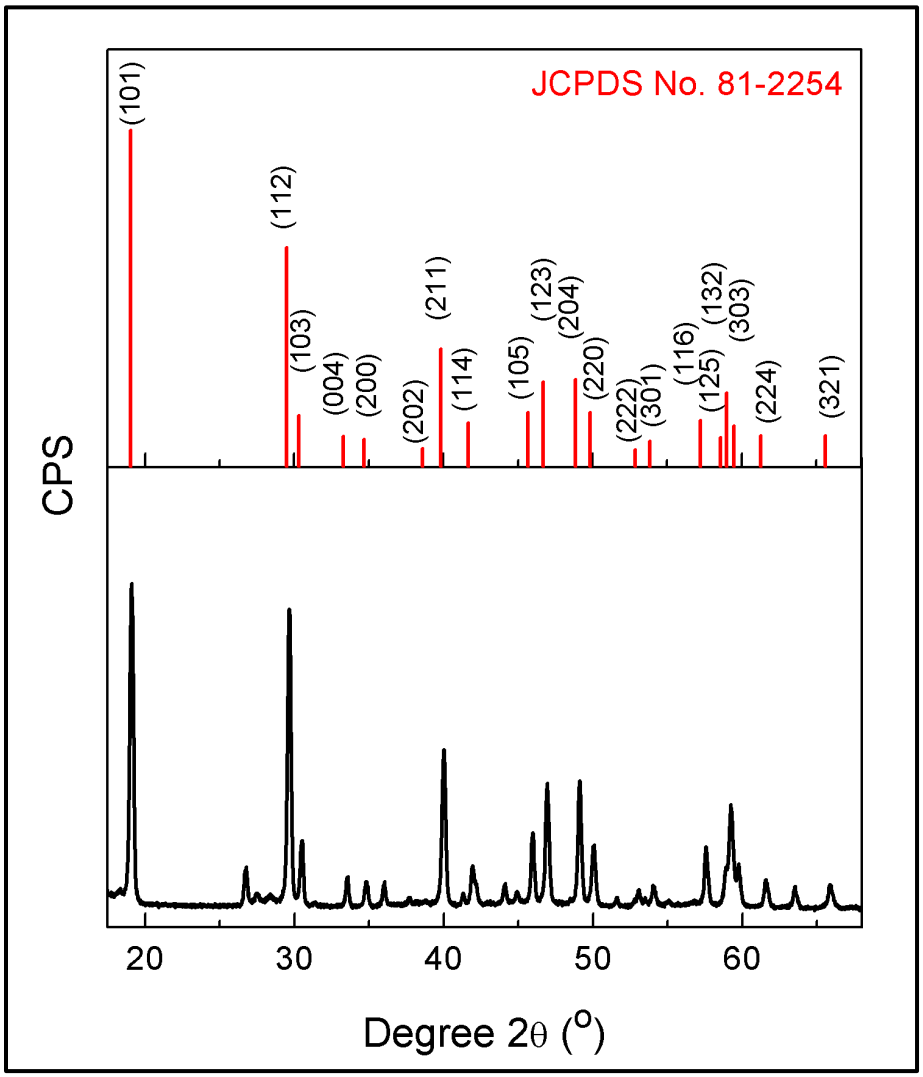

Figure 4.3. Experimental (—) and calculated standard (—) X-ray diffraction patterns for $LiYF_4$: Tm^{3+}/Yb^{3+}-UCNPs showing the tetragonal crystal phase.

4.3 Surface Characterization

Figure 4.4(i) shows the FT-IR spectra of the oleate capped UCNPs. The spectrum clearly shows that the oleate capping ligands are present on the surface of the nanoparticles. The peaks at 2933 cm^{-1} and 2857 cm^{-1} originate from asymmetric and symmetric stretching of $–CH_2$ groups, and the peaks located at 1568 cm^{-1} and 1468 cm^{-1} can be assigned to the asymmetric (δ_{as}) and the symmetric (δ_s) $–COO^-$ stretches respectively. For comparison we have included the spectrum of oleic acid (Figure 4.4 (iii)) It is worth noting that the band at 1710 cm^{-1} in the FT-IR spectrum of oleic acid corresponds to the C=O which is absent in the oleate capped nanoparticles. We conclude that for the oleate capped Ln-UCNPs the oleic acid molecules are chemically adsorbed on the Ln-UCNP through the coordination by the COO^- group of the Ln^{3+} ions on the surface. This has been observed previously for oleate capped $NaYF_4$ nanoaparticles [66].

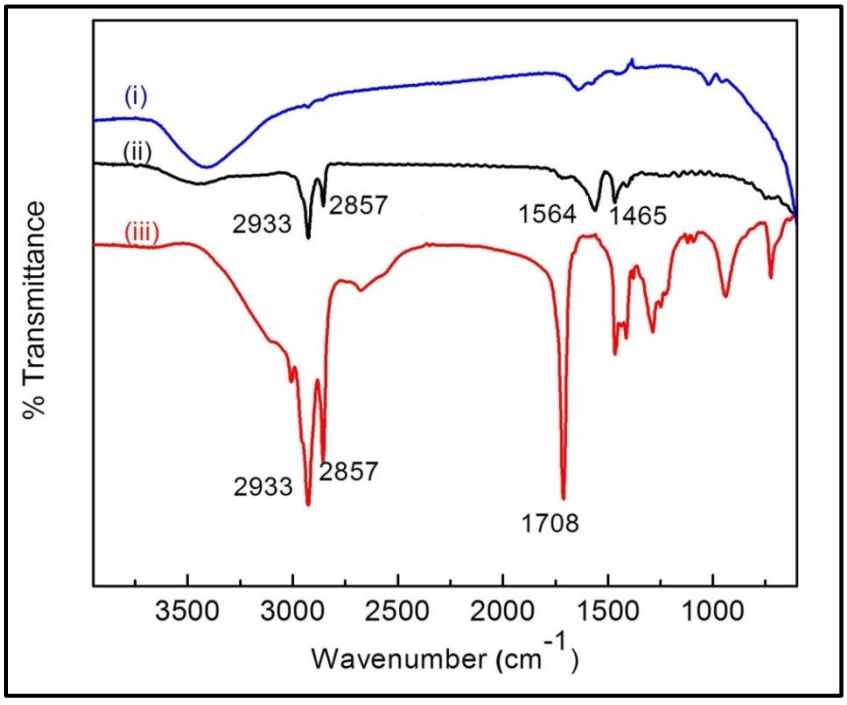

Figure 4.4. Fourier transform infrared spectra of (—) oleate-capped $LiYF_4:Tm^{3+}/Yb^{3+}$-UCNPs; (—) oleate-free $LiYF_4:Tm^{3+}/Yb^{3+}$-UCNPs; and (—) oleic acid.

4.4 Upconversion Spectroscopy

The UV, visible, and NIR upconversion emission spectrum of a 0.5 wt% solution of the oleate-capped $LiYF_4$: Tm^{3+} 0.5 mol%, Yb^{3+} 25 mol% in toluene upon irradiation with 980 nm light is shown in Figure 4.5. In the UV region two strong emission bands at 353 and 368 nm and a weaker band at 294 nm are observed. These bands are assigned to $^3P_0 \rightarrow {}^3H_6$, $^3P_0 \rightarrow {}^3F_4$, and $^1D_2 \rightarrow {}^3H_6$ respectively. In the visible region, two blue emissions bands centered at 450 and 480 nm and a red emission at 650 nm are observed. These bands are assigned to $^1D_2 \rightarrow {}^3F_4$, $^1G_4 \rightarrow {}^3H_6$ and $^1G_4 \rightarrow {}^3F_4$ transitions respectively. In the NIR region, a strong emission centered at 800 nm corresponding to the transition $^3H_4 \rightarrow {}^3H_6$ is observed. This emission band could be used in biomedical applications such as in bioimaging.

The upconversion mechanism for $LiYF_4$:Tm^{3+}/Yb^{3+} is shown in Figure 4.6 and has been reported previously by our group [25]. It is important to mention here the fact that the UV emissions require several incident photons (NIR) suggesting that $LiYF_4$ is an efficient matrix at the nanoscale, compared to other fluorides or oxides matrices for Ln^{3+} doping, in particular for Tm^{3+} ions. For example, the emission at 290 nm requires at least five incident photons to populate the $^3P_0$ emitting level, which is not observed when the Tm^{3+} ions are doped in the much studied $NaYF_4$ matrix or other Tm^{3+} doped nanoparticles. This supports the conclusion that $LiYF_4$ is an efficient matrix for upconversion.

To reduce the cross-relaxation energy loss in the upconversion, the concentration of Tm^{3+} ions are generally kept very low, 0.5 mol% in this case, so that all the Tm^{3+} ions could be isolated in the nanoparticles and no energy would be transferred among them.

Unlike the activator, the sensitizer is usually present in a higher concentration in the nanoparticles. Yb^{3+} ions are good sensitizers due to the large absorption cross-section in the NIR region arising from the $^2F_{7/2} \rightarrow {}^2F_{5/2}$ transition (Figure 4.6), which is also resonance with the *f-f* transition of Tm^{3+} thus enable the energy transfer from Yb^{3+} to Tm^{3+} in the upconversion process.

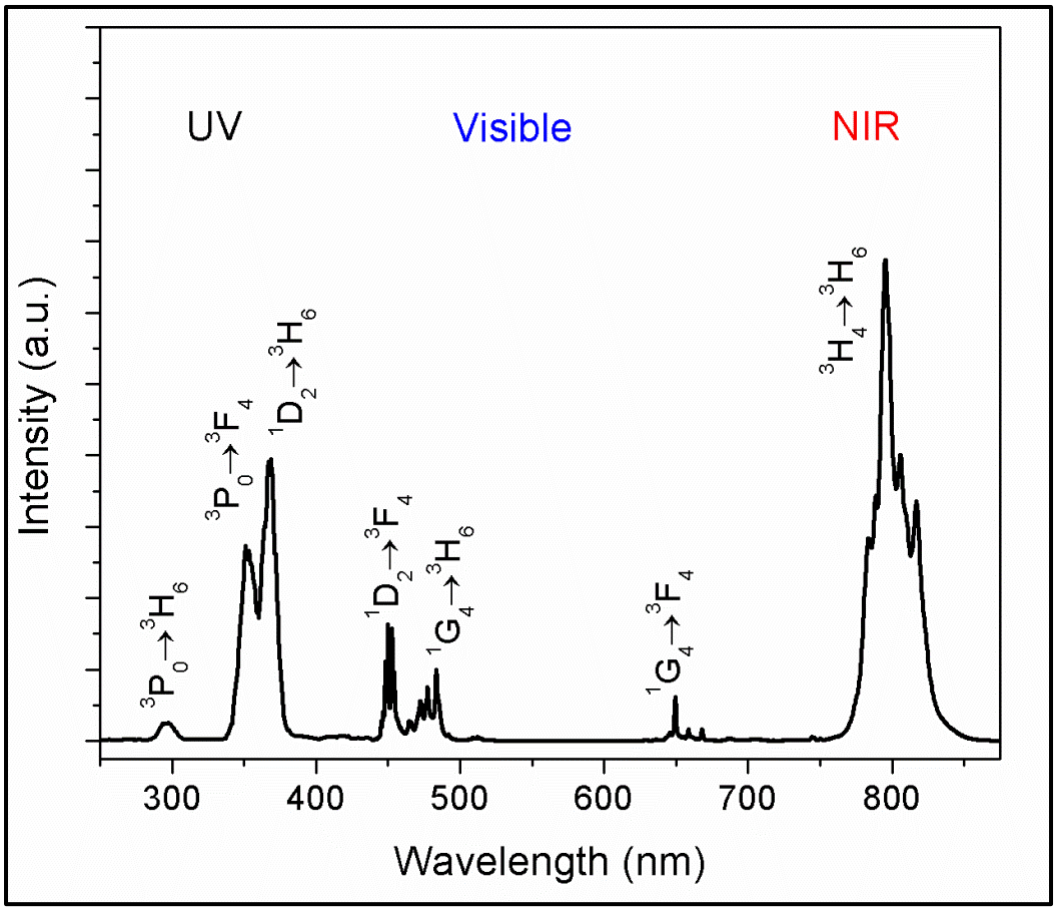

Figure 4.5. Upconverting luminescence emission spectrum of $LiYF_4$: Tm^{3+}/Yb^{3+}-UCNPs from UV to NIR region (0.5 wt% in toluene).

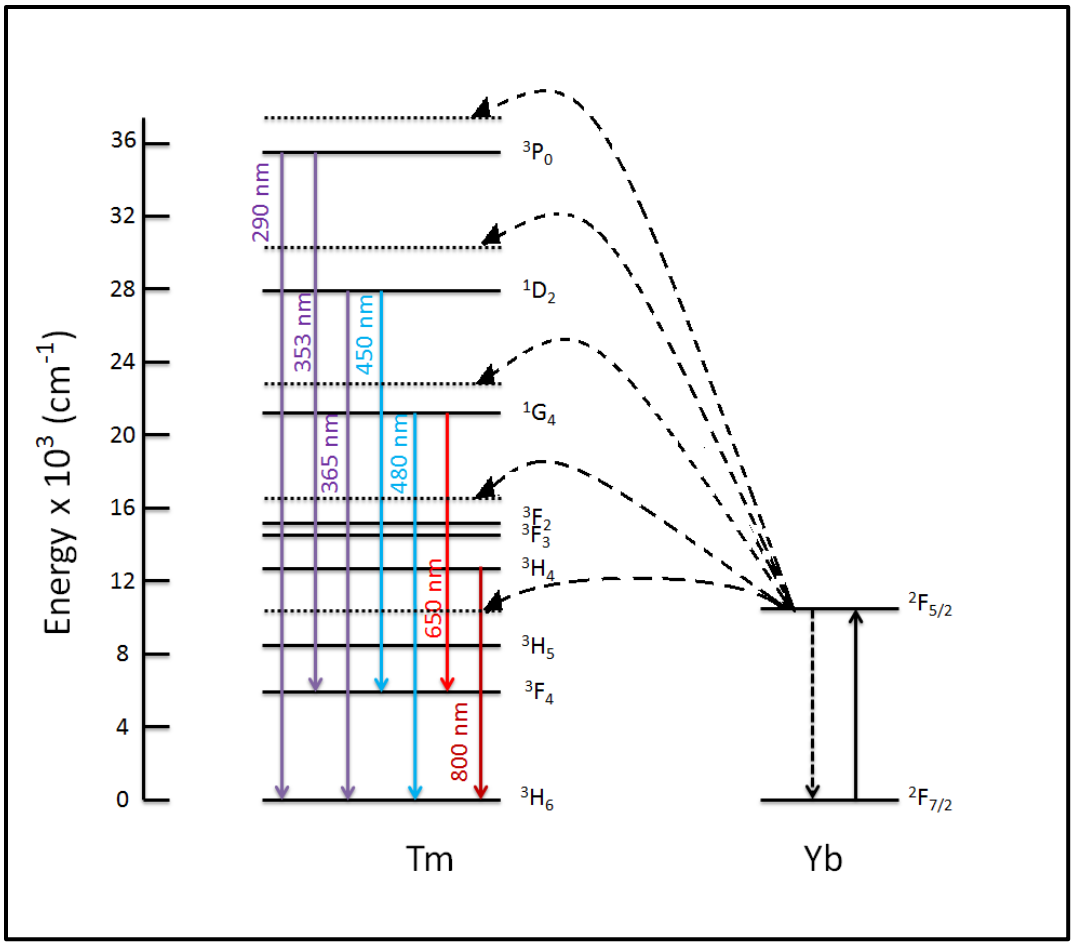

Figure 4.6. Schematic representation of the possible energy transfer processes responsible for the generation of UV to NIR emissions from $LiYF_4$: Tm^{3+}/Yb^{3+}-UCNPs *via* upconversion.

Chapter Five – Modification and Characterization of the Novel Photosensitizers m-THPC-MBA

The photosensitizer Temoporfin (5,10,15,20-tetra(m-hydroxyphenyl) chlorin, m-THPC, or Foscan®) is a commercially available drug widely used in the treatment of head and neck cancers. As a second generation photosensitizer it has an enhanced absorption of light in the red that has been found to be more effective than conventional porphyrins and reduces the skin photosensitization which is a side effect associated with PDT. The absorption of photosensitizers is an essential aspect to consider in the development of PDT and the work present in this thesis aimed to use the NIR light as the excitation source *via* conjugating the photosensitizer on the lanthanide-doped upconverting nanoparticles, $LiYF_4:Tm^{3+}/Yb^{3+}$-UCNPs, so that the photodynamic therapy can be applied in "deep" tissues. To facilitate the conjugation with upconverting nanoparticles, the photosensitizer m-THPC needed a modification which facilitates the conjugation of m-THPC to the nanoparticles and give rise to a shift of the Soret band in order to maximize the overlap of this band with the blue emission band of the UCNPs. Computational studies were carried out to ascertain the position of the linker and the effect on the absorption spectrum of m-THPC.

The second part of the work consisted of the study of the potential of m-THPC-MBA(III)-$LiYF_4:Tm^{3+}/Yb^{3+}$-UCNPs to generate singlet oxygen and studies on cell viability.

5.1 Modification of the Photosensitizer

The photosensitizer m-THPC is a porphyrin derivative that has a macrocycle ring with four phenoxyl groups attached in the *meso* positions. The structure shows that m-THPC lacks appropriate functional group(s), which would allow it to be conjugated to the UCNPs. In addition, the as-synthesized UCNPs are capped with oleate, which does not react with the photosensitizer. In order to conjugate m-THPC to the UCNPs both must be modified. An acid treatment developed in our laboratory to remove the oleate ligand from their surface (see Chapter 4) was employed, which facilitates the direct conjugation of electronegative groups rendering the UCNPs amenable to m-THPC functionalization [66]. In addition, the m-THPC required modification to introduce an appropriate negatively charged group to bond to the ligand-free UCNPs positively-charged surface. In order to modify the m-THPC, 4-(bromomethyl)benzoic acid (BMBA) was used as it is a commonly used "linker" in biological applications that is generally recognized as non-harmful to tissues and organs and provides the required carboxylate functionality (-COO-) to bond to the surface of the nanoparticles.

The methyl benzoic acid (MBA) linker was covalently bonded to the m-THPC using the coupling reaction shown in Scheme 5.1. In the reaction the strong base NaH, having H_2 as its conjugate acid with a pK_a of 35,0 was employed to deprotonate the phenol (pK_a 10) and amine (pK_a 17.5) groups of m-THPC. Deprotonation renders m-THPC nucleophilic which favors the substitution reaction with 4-(bromomethyl)benzoic acid to produce three possible products m-THPC-MBA (I), m-THPC-MBA (II), and m-THPC-MBA (III). Therefore, it is important to ascertain the number and position of the linkers. The two isomers m-THPC-MBA (I) and m-THPC-MBA (II) have linker on the phenyl

group “outside” the chlorin whereas for m-THPC-MBA (III) the linker is shown as being added to the nitrogen in the chlorin ring. Scheme 5.2 shows the mechanism, which could lead to the deprotonation of the pyrrole followed by a nucleophilic attack of the linker to form m-THPC-MBA (III). It should be noted that m-THPC possesses a plane of symmetry (Scheme 5.1) therefore the substitutions that occur on the left side of m-THPC are equivalent to those on the right side, thus resulting in only three possible isomers.

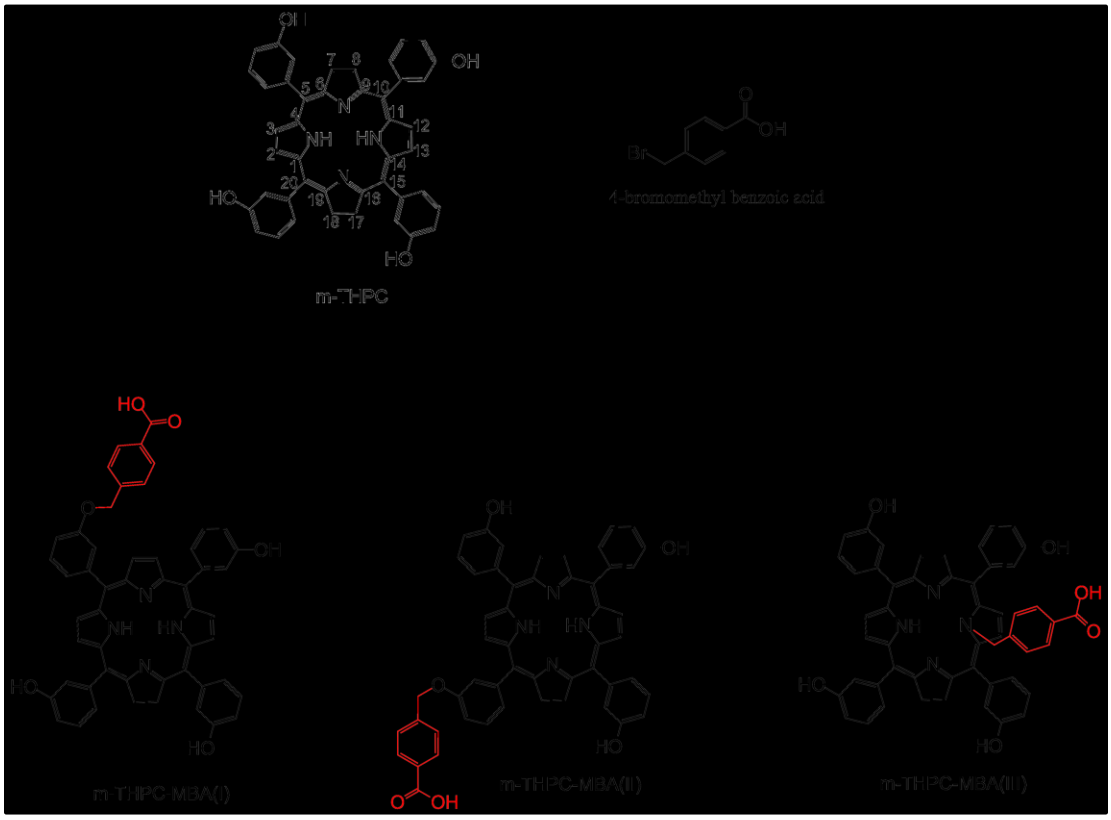

Scheme 5.1. Conversion of m-THPC to m-THPC-MBA (I), (II), and (III) endowing a carboxylic acid functionality to the latter and allowing for the molecule to cap the positively charged nanoparticles surface.

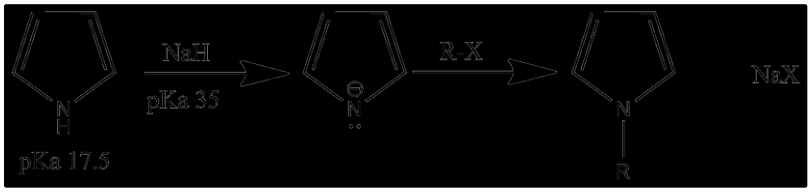

Scheme 5.2 Deprotonation of pyrrole group using sodium hydride followed by substitution reaction.

5.1.1 Absorption Spectroscopy of the Modified Photosensitizer

The coupling reaction of m-THPC and 4-(bromomethyl)benzoic acid produced a green colored product. UV/Vis spectra of m-THPC and of the product m-THPC-MBA shown in Figure 5.1 were carried out in an ethanol/propylene glycol mixture, which is the solvent suggested by the European Medicines Evaluation Agency (EMEA) to be used for the injection of m-THPC in humans. A comparison between the spectrum of the unsubstituted parent and the product (m-THPC-MBA) showed three distinct differences, namely a red shift of the Soret band from 417 nm (parent) to 438 nm (green product), a lower molar absorption coefficient at λ_{max} (ε=1.05 x 10^4 $cm^{-1}M^{-1}$), peak broadening and the disappearance of two of the Q-bands in the 500 nm region and of the peak at 650 nm.

The number of linkers and their position(s) bonding to the m-THPC was expected to shed light on the possible reasons for the observed spectral difference. In the following sections experimental and computational results are presented and discussed to explain the effect of the linker on the observed spectral differences of m-THPC.

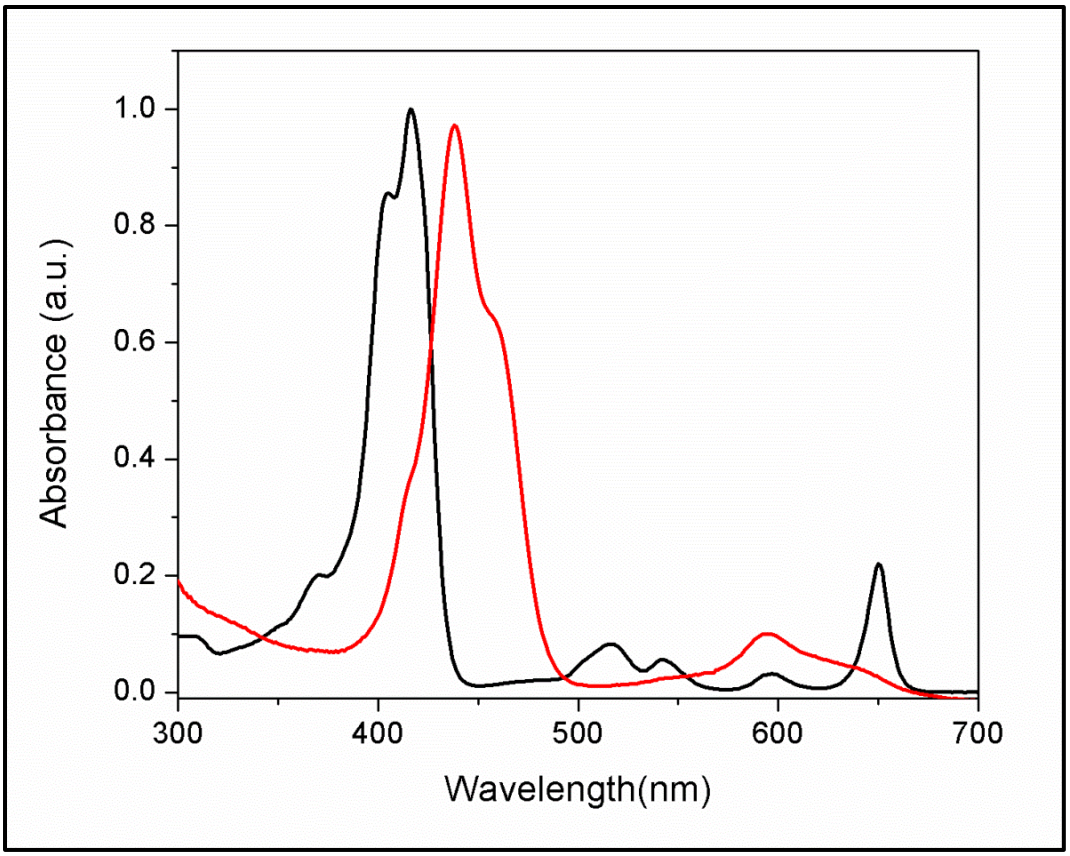

Figure 5.1. UV/Vis spectra of (—) m-THPC and (—) the m-THPC-MBA product (green color) measured in an ethanol/propylene glycol mixture solvent.

5.1.2 Isolation and Characterization of m-THPC-MBA

The product from the coupling reaction may be a mixture as postulated in Section 5.1. Thus it was necessary to ascertain the number and the position of the "linker(s)" bonding to the m-THPC. The number of linkers bonded to m-THPC was investigated using liquid-chromatography mass spectroscopy (LC-MS) and the results (Figure 5.2) showed the product is a mixture consisting of three different compounds with 1 to 3 methyl benzoic acids bonded to m-THPC. Using centrifugal thin-layer chromatography it was found that the major product (58% of the total) has one linker bonded to m-THPC and the two minor products, which constitute 15% and 11% of the total and have two and

three "linkers" respectively bonded to m-THPC. The rest 16% is the unreacted reagent m-THPC.

The major product was isolated and characterized by LC-MS and showed two main peaks, having a molecular ion peak at 815, which corresponds to only one linker bonded to m-THPC. To isolate these two isomers further purification was carried out using preparative liquid chromatography using a reversed phase column and characterized by mass spectrometry. The elution profile (Figure 5.3) of the products with molecular ion peaks at 815 showed two main bands with retention times of 7.5 min and 10.1 min, indicating the presence of at least two isomers with different structure.

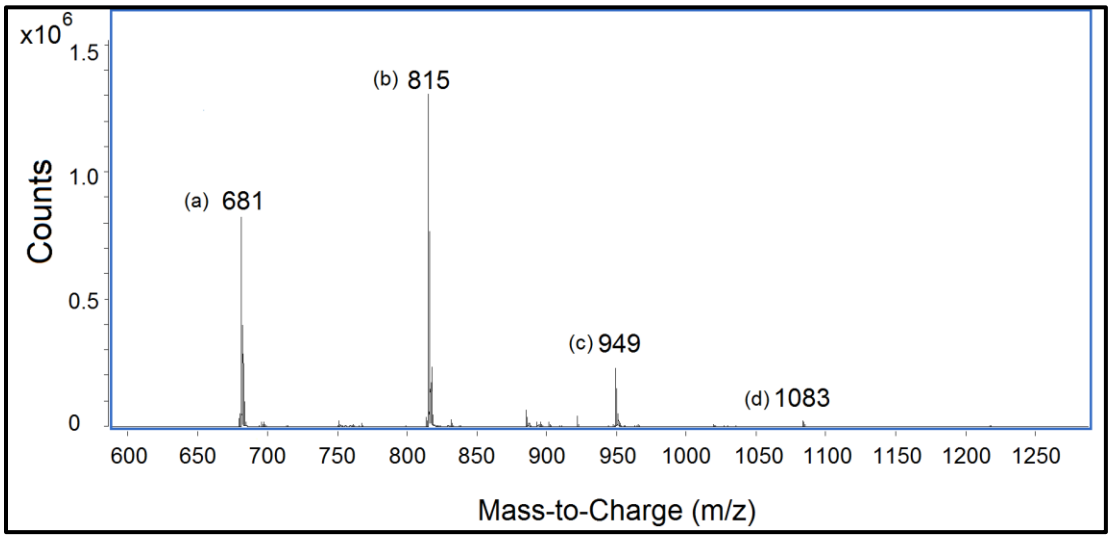

Figure 5.2. LC-MS results of the products from the coupling reaction. The spectrum shows four compounds; (a) m-THPC, (b) m-THPC-MBA with one linker, (c) m-THPC-MBA with 2 linkers and (d) m-THPC-MBA with 3 linkers.

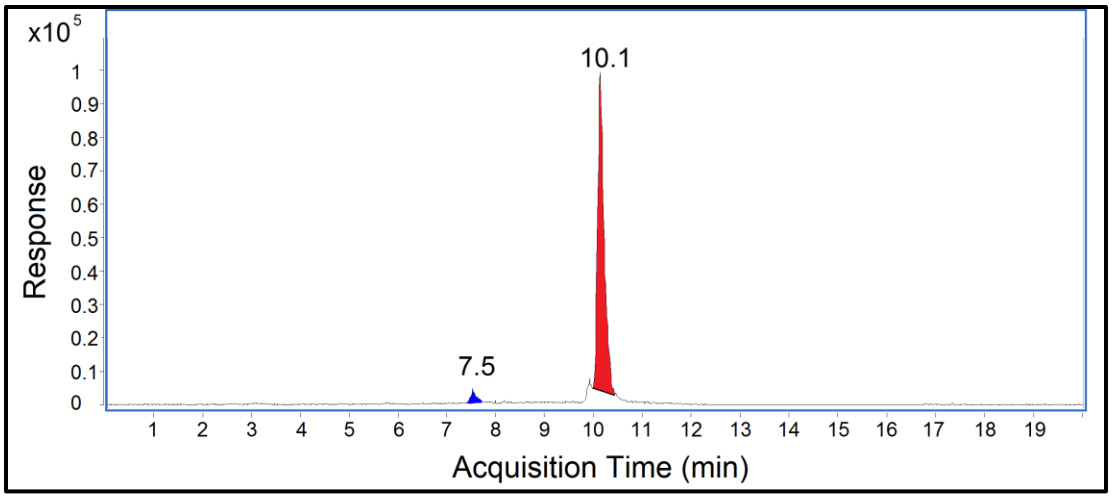

Figure 5.3. Elution profile from Prep LC-MS. Isomers m-THPC-MBA (I) and (II) with molecular weight of 815 were eluted at retention time 10.1 min, and isomer m-THPC-MBA (III) was eluted at 7.5 min.

UV/Vis absorption spectra of the two eluted fractions were measured in a solution of ethanol/propylene glycol and compared to the spectrum of m-THPC. The resulting spectra are shown in Figure 5.4. The fraction that has an elution time of 10.1 min demonstrated excellent correspondence with the absorption spectrum of the m-THPC, whereas the fraction with an elution time of 7.5 min showed a red shift in comparison to m-THPC.

Three possibilities may be put forward to explain the red shift. Firstly, the addition of methyl benzoic acid to m-THPC serves as an electron-donating group, which changes the electron distribution of the porphyrin. Increasing the electron density lowers the energy gap between the ground and excited state resulting in absorption at the longer wavelength. Secondly, the observed changes may be due to the aggregation of the m-THPC molecules that has been reported previously [69]. m-THPC molecules are hydrophobic and tend to aggregate in polar solvents or in an aqueous environment. The

aggregation of m-THPC has been attributed to hydrogen bonding of the peripheral phenyl groups of the m-THPC molecules. This results in a chain like structure (J-type) that is characterized by a large offset between the line connecting the centres and the direction of the transition dipoles in two neighbouring molecules. However, aggregation can be eliminated as the cause for the red shift since it has been shown to occur when the concentration of m-THPC exceeds 10^{-4} M in ethanol or the solvent contains more than 50% volume ratio of water [70, 71]. The experiments in this study were carried out at a concentration of 10^{-5} M m-THPC in an ethanol/propylene glycol mixture. Thirdly, at the pH of the medium (pH lower than the pK_a of the imino groups: pK_3=3.45 and pK_4=1.45), the nitrogens are protonated and thus the m-THPC molecules will be positively charged resulting in an observed red shift [69]. However, since all the experiments were performed using the physiological pH of 7.4, the pH of the medium is not a plausible explanation for the observed red shift. At this point we postulate that the red shift of the Soret band in the absorption spectrum of m-THPC-MBA (III) is strictly due to the addition of 4-(bromomethyl)benzoic acid, which acts as an electron donating group.

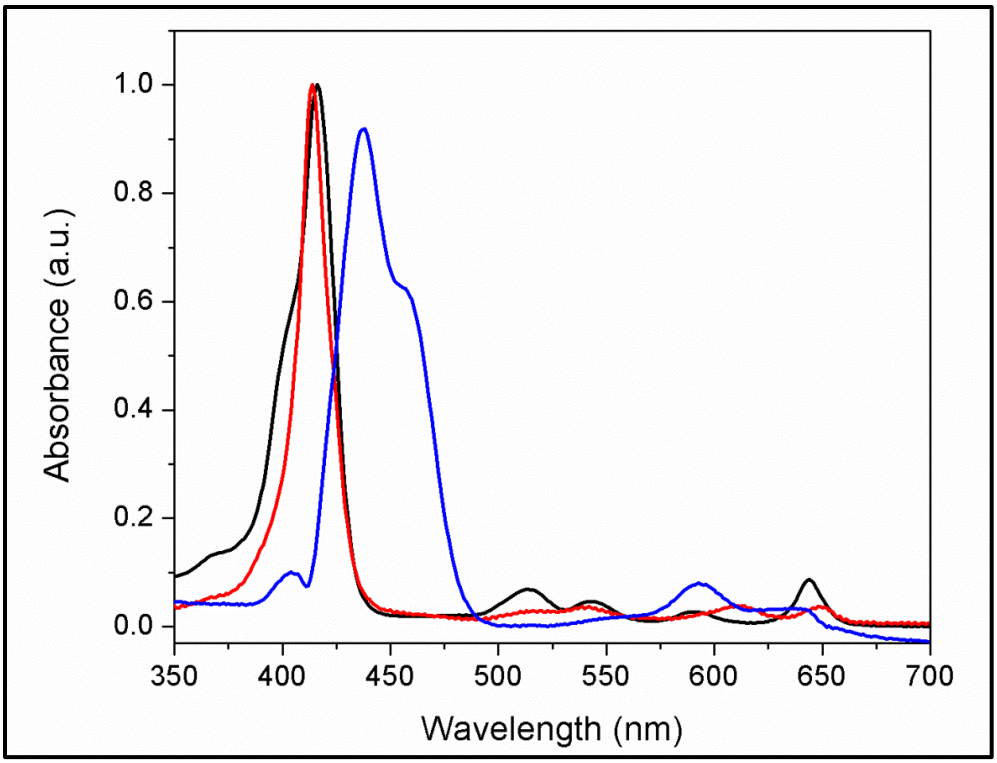

Figure 5.4. UV/Vis absorption spectra of (—) m-THPC, (—) m-THPC-MBA (I) and (II) isomers eluted at 10.1 min and (—) m-THPC-MBA (III) isomers eluted at 7.5 min from Prep LC-MS. All three spectra were measured in ethanol/propylene glycol mixture solvent.

5.2 Computational Studies of m-THPC and m-THPC-MBA

It has been well documented that changes in the conjugation pathway and symmetry of porphyrin can affect its UV/Vis absorption spectrum. The absorption spectrum of porphyrin has long been understood in terms of the highly successful four orbital model first applied by Gouterman [59, 60]. The method demonstrated the importance of charge localization on electronic spectroscopic properties and the absorption bands of porphyrin all arise from the transitions between two HOMOs and two LUMOs. It is well recognized that *time dependent density functional theory* (TD-DFT) methods can be used successfully to study the electronic structure and spectral properties of porphyrin and

related compounds [57, 58]. Thus, to understand the observed spectral changes (effect of substituent and its position) such as red shift of Soret band on the modified m-THPC-MBA, a computational study was carried out using Gaussian 09 program [72]. In the calculations *time-dependent density functional theory* (TD-DFT) was combined with Becke Three Parameter Hybrid Functionals (B3LYP) and the basis set 6-31G(d,p) was used to optimize the ground state geometry of the four of the m-THPC and m-THPC-MBA as well as to simulate the absorption spectra [73, 74]. The solvent effect of ethanol was simulated using the CPCM (conductor-like polarizable continuum model) [75, 76]. The models used, m-THPC-MBA (I), m-THPC-MBA (II), m-THPC-MBA (III), shown in Scheme 5.1 are based on the possible reactive sites of m-THPC.

5.2.1 Molecular Structure *via* Geometry Optimization

In computational analysis it is imperative to perform geometry optimization on the molecules of interest before carrying out any other calculations since structural changes of a molecule could lead to changes in its energy and other properties. The ground state geometry of m-THPC and the three modified m-THPC-MBA isomers were optimized and their optimized geometries were verified to be local minima by frequency calculations. The calculations from all four models show that the chlorin macrocycle is planar and the four phenyl groups at positions 5, 10, 15, 20 do not lie planar to the chorin macrocycle, but are positioned in ~60° angle (Figure 5.5). It has been previously shown that this geometrical arrangement of the phenyl groups is responsible for only a minor shift of the absorption bands compared to chlorin itself [77].

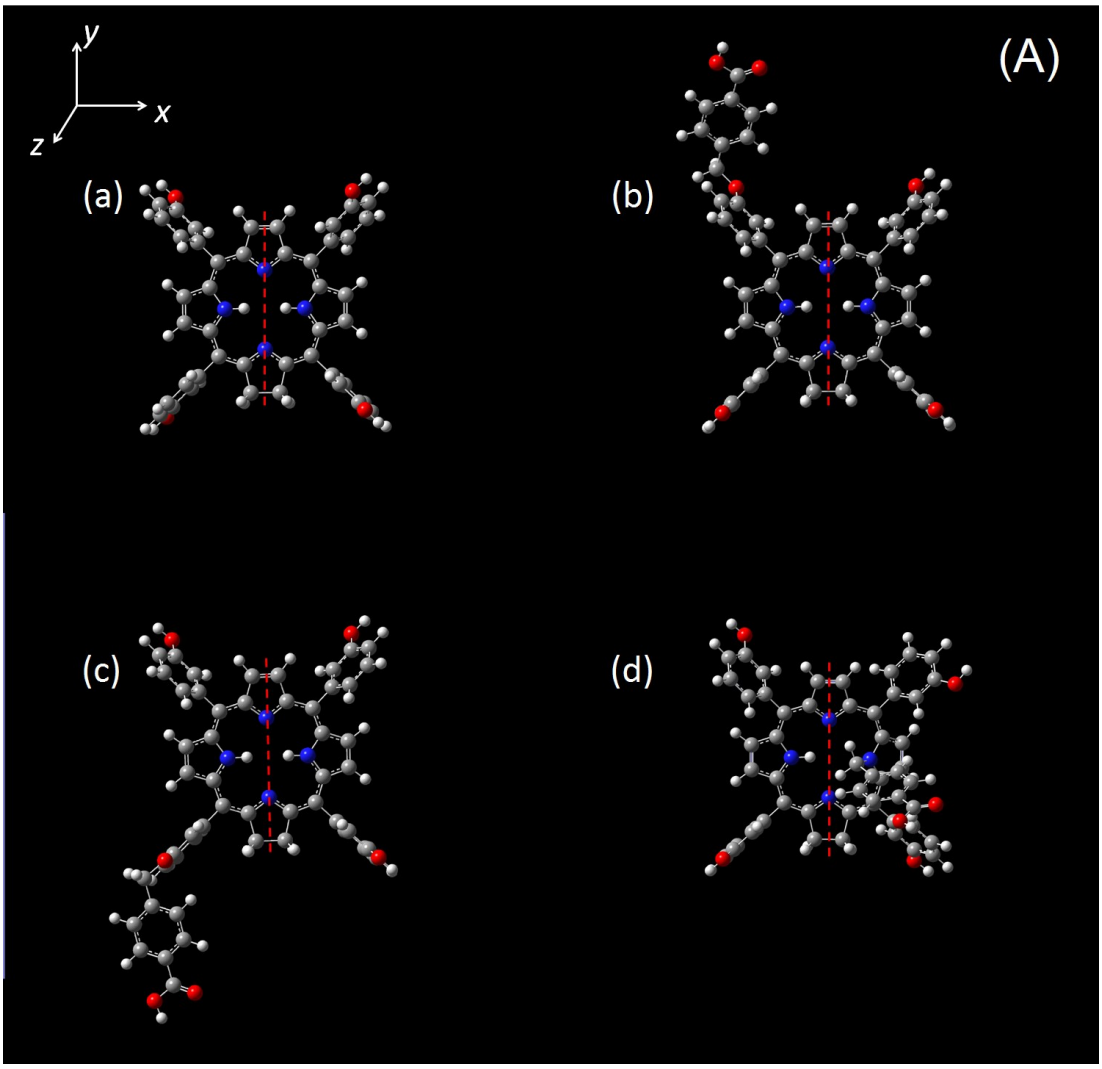

Figure 5.5. The ground-state molecular structures of (a) m-THPC, (b) m-THPC-MBA (I), (c) m-THPC-MBA (II), and (d) m-THPC-MBA (III) optimized at the TD-DFT/B3LYP level. The red dash line passing through the two pyrroles (----) represents the yz-plane of symmetry.

For the modified m-THPC-MBA (I) and m-THPC-MBA (II) where the methyl-benzoic acid linker is added to the phenyl groups at positions 5 and 20 respectively, the linker is at an angle of ~27° from the xy-plane and parallel to the chlorin macrocycle as indicated in Figure 5.6. For m-THPC-MBA (III) where the linker has added to the

nitrogen in the chlorin ring, it was found to be at an angle of 67° to the chlorin macrocycle. More importantly, the two nitrogen atoms of the pyrrole move upwards from the xy-plane and as a consequence the chlorin ring is distorted and thus the symmetry of the macrocycle is broken.

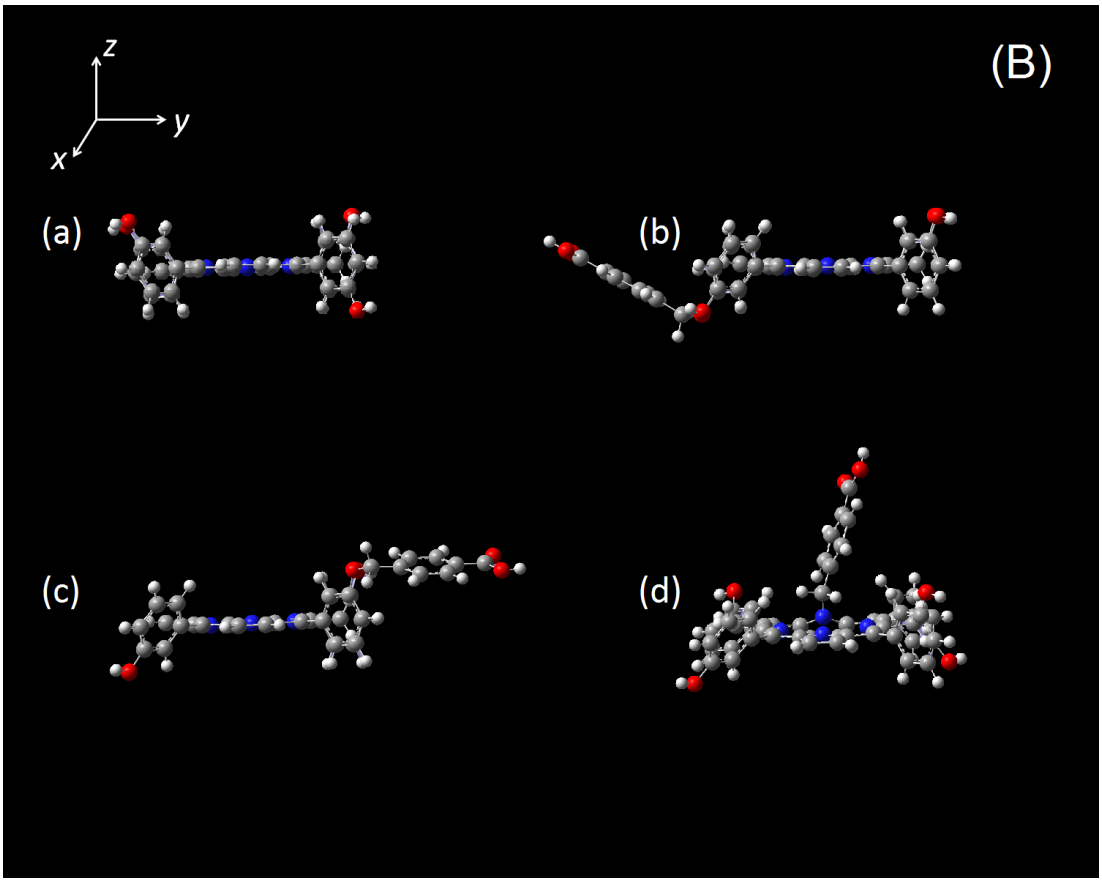

Figure 5.6. The structures of the ground state viewed from the y-axis showing the side-view of the geometry. Three of the molecules (a, b, c) have a planar chlorin ring while in (d) the chlorin ring is not planar due to the addition of the linker directly onto the ring.

5.2.2 Computational Studies of Excited State Electronic Structure and Absorption Spectroscopy

The chlorin macrocycle is the reduced form of porphyrin with a saturated bond between C17 and C18. Gouterman's four orbital model was applied to calculate the absorption spectra of m-THPC and of the three isomers of m-THPC-MBA. The four orbital model has shown that the absorption bands of chlorin arise from transitions between two HOMOs and two LUMOs. The energies associated within these orbitals are very important factors that influence the transitions thus the resulting absorption spectra. Figure 5.7 shows the calculated four molecular orbitals from HOMO -1 to LUMO +1 for m-THPC and the three isomers. The calculated molecular orbitals of the chlorin ring show no difference between m-THPC, m-THPC-MBA (I), and m-THPC-MBA (II). Whereas for m-THPC-MBA (III) the π-orbitals between carbon 10 and 11 (in HOMO-1) and between carbon 8 and 9 (in HOMO) have a larger volume compared with the same orbitals for m-THPC and m-THPC-MBA (I) and m-THPC-MBA (II). The changes in the molecular orbitals are reflected in their energies as illustrated in the partial molecular orbital diagram in Figure 5.8.

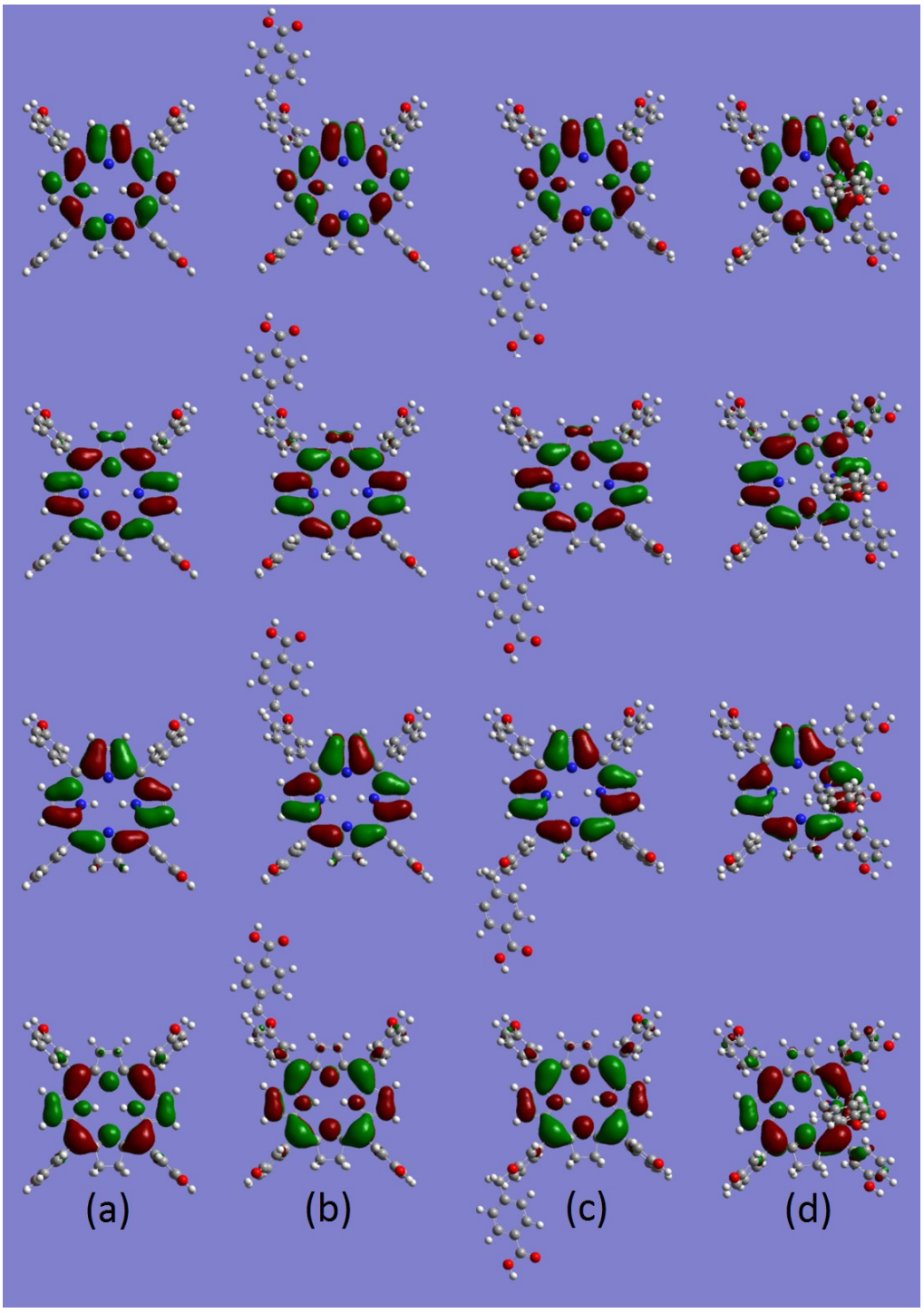

Figure 5.7. Calculated molecular orbitals (from bottom to top, HOMO -1 through LUMO +1) for (a) m-THPC, (b) m-THPC-MBA (I), (c) m-THPC-MBA (II), and (d) m-THPC-MBA (III). The electron density is shown as the balloons in red (positive wavefunction) and green (negative wavefunction).

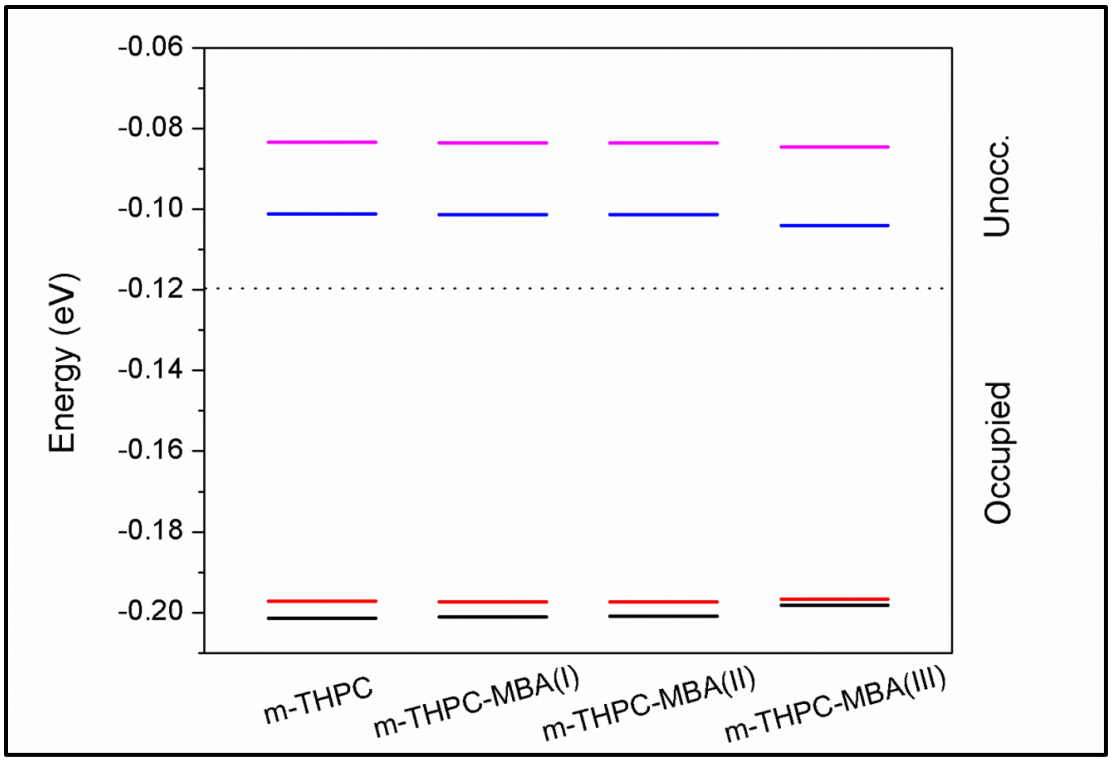

Figure 5.8. Partial molecular orbital diagrams from HOMO -1 to LUMO +1 of m-THPC, m-THPC-MBA (I), m-THPC-MBA (II) and m-THPC-MBA (III) calculated by TD-DFT in liquid phase using CPCM solvation model.

Transitions between two HOMOs and two LUMOs give rise to two excited states and orbital mixing splits these two states producing a higher energy state with a higher oscillator strength (Soret band) and a lower energy state with lower oscillator strength (Q-bands). In case of chlorin system the absorption bands are mainly due to the lowest four excited singlet states from S_1 to S_4. A total of 15 transitions were used to calculate the absorption spectra for m-THPC and the three isomers m-THPC-MBA. As shown in Figure 5.9 the Soret bands B_1 and B_2, 3rd and 4th excited singlet state, respectively, are for the transitions between HOMOs and LUMOs in which the dipole moments are in the same direction, therefore resulting in higher energy and intensity. The Q-bands Q_1 and Q_2

correspond to the excitations from the ground singlet state to the first and second excited singlet states. Since the transitions between HOMOs and LUMOs that generate the two Q-bands have dipole moments with opposite direction, these transitions show are much weaker and at lower energy. In Table 5.1 the calculated excitation energies and the oscillator strengths of m-THPC and three m-THPC-MBA isomers are summarized. The results reveal a bathochromic shift in the Soret band of the m-THPC-MBA (III) compared with the excitation energies calculated for m-THPC and m-THPC-MBA (I) and (II).

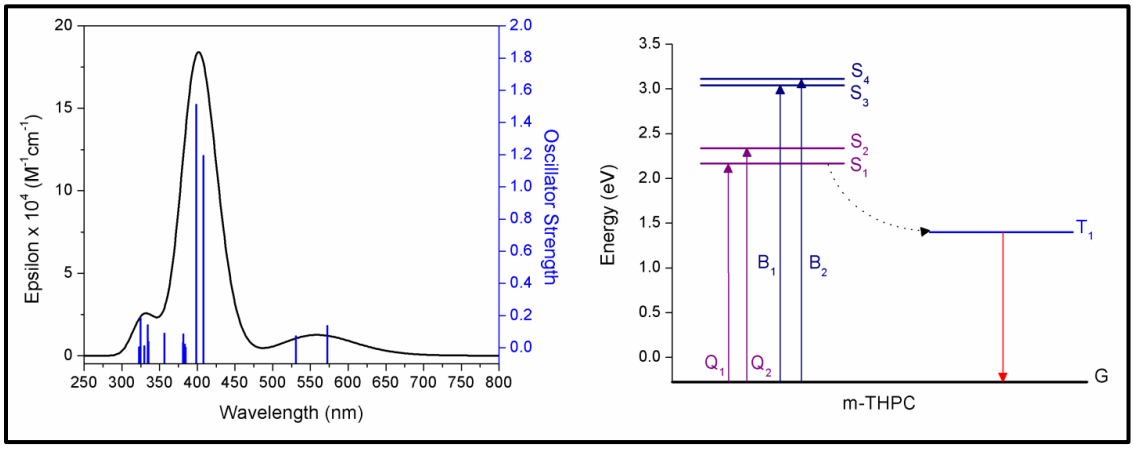

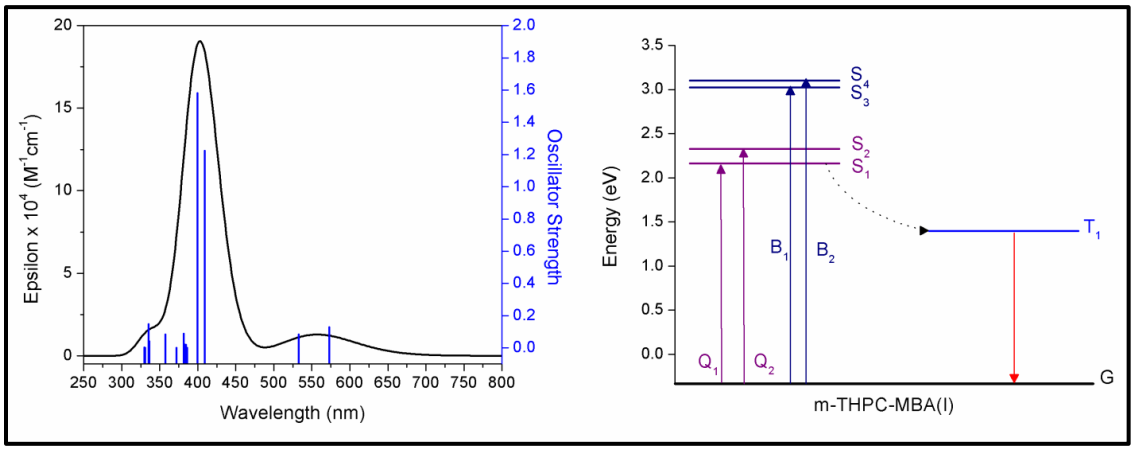

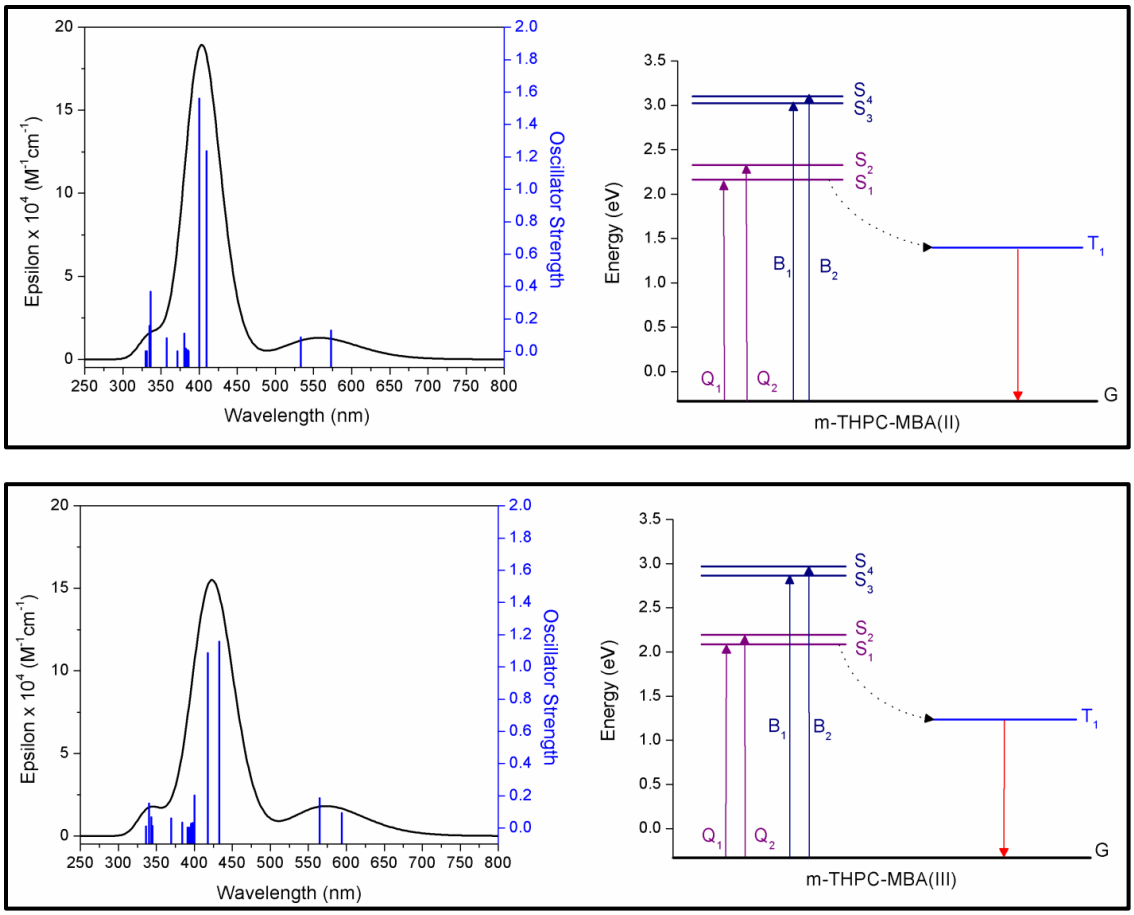

Figure 5.9. The simulated absorption spectra and excited state diagram of m-THPC, m-THPC-MBA (I), m-THPC-MBA (II), and m-THPC-MBA (III). The 15 transitions responding for the absorption bands were calculated and shown as the blue bars in the spectra.

Table 5.1 Calculated excitation energies and oscillator strengths of m-THPC, m-THPC-MBA (I), m-THPC-MBA (II), and m-THPC-MBA (III) in EtOH using TD-DFT/B3LYP.

State		Wavelength (nm)	Excited Energy (eV)	Oscillator Strength
m-THPC	S_1	572.11	2.1671	0.1360
	S_2	530.75	2.3360	0.0727
	S_3	408.05	3.0384	1.1918
	S_4	398.47	3.1115	1.5092
	T_1	884.86	1.4012	n/a
m-THPC-MBA (I)	S_1	572.66	2.1651	0.1292
	S_2	532.57	2.3280	0.0838
	S_3	409.29	3.0292	1.2229
	S_4	399.56	3.1030	1.5805
	T_1	886.65	1.3984	n/a
m-THPC-MBA (II)	S_1	573.01	2.1637	0.1293
	S_2	533.12	2.3256	0.0853
	S_3	409.83	3.0253	1.2347
	S_4	399.83	3.1009	1.5605
	T_1	887.61	1.3968	n/a
m-THPC-MBA (III)	S_1	593.73	2.0882	0.0937
	S_2	564.90	2.1948	0.1863
	S_3	432.71	2.8653	1.1580
	S_4	417.85	2.9672	1.0851
	T_1	1005.58	1.2330	n/a

The calculated electronic absorption spectra (in ethanol) of the three isomers and m-THPC are shown in Figure 5.10. There is an excellent overlap between the calculated absorption spectra of m-THPC, m-THPC-MBA (I) and m-THPC-MBA (II). More importantly the calculated absorption spectrum of m-THPC-MBA (III) shows a bathochromic shift of the Soret band which is in excellent agreement with the experimental absorption spectrum. The linker MBA is an electron donor thus we would expect a change in electron density in the temoporfin molecule, which may affect the absorption spectrum. However, the simulation results for the two isomers m-THPC-MBA (I, II) clearly show that the addition of MBA has no effect on the absorption properties. The linker is 6.16 Å from the chlorin ring, in addition there is an isolating group, $-CH_2-$,

between the carboxyphenyl and the phenyl ring, therefore the linker is not conjugated to the chlorin ring and has no influence on the absorption properties. In contrast, the addition of the linker on the nitrogen in the chlorin ring results in a bathochromic shift of the Soret band. In this case the proximity of methyl benzoic acid to the conjugated system increases the electron density resulting in a decrease of the energy gaps between the HOMO and the LUMO, which manifests itself as a red shift of the Soret band. The distortion of the chlorin ring caused by the addition of the MBA may also contribute to the bathochromic shift. The computational results have allowed us to determine m-THPC-MBA (III) to be the product isolated, which is responsible for the red shift of the Soret band from 417 nm to 438 nm.

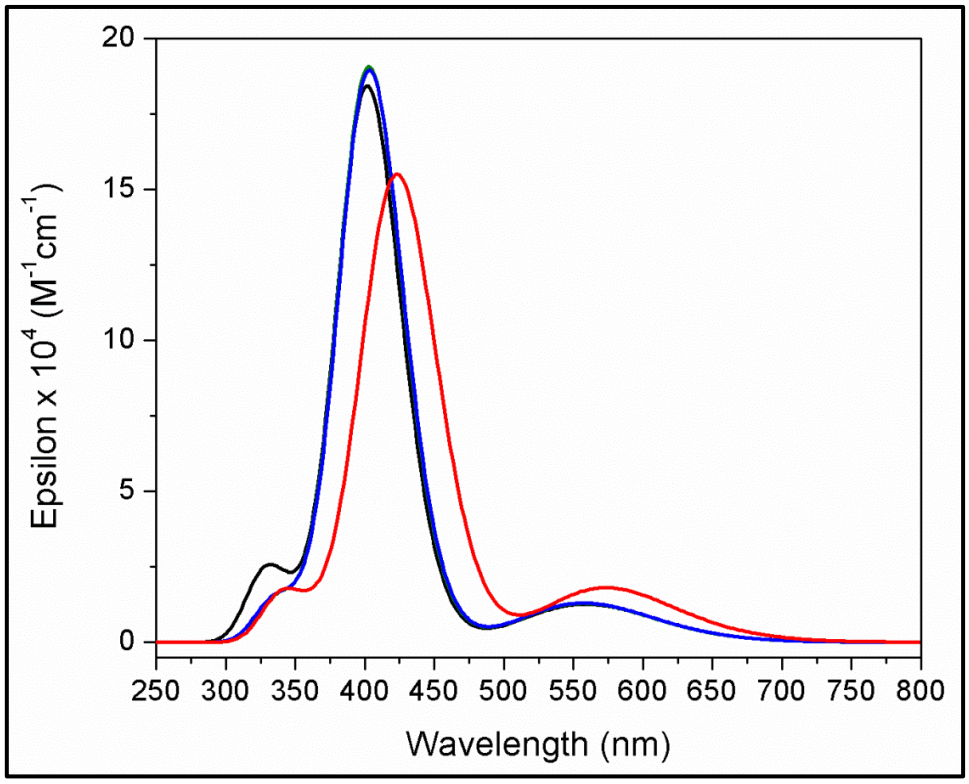

Figure 5.10. The simulated absorption spectra of (—) m-THPC, (—) m-THPC-MBA (I), (—) m-THPC-MBA (II) and (—) m-THPC-MBA (III) calculated by TD-DFT/B3LYP in

ethanol using CPCM solvation. The spectra of m-THPC-MBA (I) and m-THPC-MBA (II) are indeed overlapped.

5.3 Calculation of the Triplet Excited State of m-THPC and m-THPC-MBA Isomers

A good photosensitizer must be able to generate singlet oxygen. This is determined by the energy of the excited triplet state T_1. The singlet excited state may decay to the ground state *via* spin inversion and populate the T_1 through intersystem crossing (ISC). The energy gap between the ground singlet state G and the excited triplet state T_1 must be larger than 0.98 eV in order to excite oxygen from its ground triplet state to the first singlet state $^1\Delta_g$ [32]. Using TD-DFT/B3LYP methods the 1st triplet state excitation energies of m-THPC and m-THPC-MBA isomers were calculated and are summarized in Table 5.2.

Table 5.2 Energies of the ground singlet state and the difference between the ground singlet state and the first excited triplet state optimized with various methods.

Compound	Ground Singlet State (eV)	TD-DFT/B3LPY	
		CPCM	Gas
m-THPC	-0.2747	1.68	1.66
m-THPC-MBA(I)	-0.3316	1.73	1.72
m-THPC-MBA(II)	-0.3316	1.56	1.56
m-THPC-MBA(III)	-0.3316	1.73	1.72

The calculations were performed in both gas phase and liquid phase (ethanol) using CPCM. The excited triplet energies in both phases showed very similar results and were all higher than the required 0.98 eV. Therefore, the computational results show that adding the linker on the chlorin ring *via* the nitrogen atom does not affect the photosensitizer's ability in singlet oxygen production.

Chapter Six - Conjugation of m-THPC-MBA (III) to $LiYF_4$: Tm^{3+}/Yb^{3+} Nanoparticles

The modified photosensitizer m-THPC-MBA (III) which shows the red shift of the Soret band was functionalized onto the surface of ligand-free $LiYF_4$:Tm^{3+}/Yb^{3+}-UCNPs. The functionalization was carried out at neutral pH. At this pH ligand-free $LiYF_4$:Tm^{3+}/Yb^{3+}-UCNPs possess a positive charges on their surface and the carboxylate group of the photosensitizer m-THPC-MBA (III) has a negative charges. The resulting nanoconstruct (m-THPC-MBA (III)-UCNP) showed a green color, had very good dispersibility in ethanol/propylene glycol solution and it is stable for months. It was found there are 7.6 x 10^3 molecules of m-THPC-MBA (III) on each UCNP. A schematic illustration of the nanoconstruct is shown in Figure 6.1.

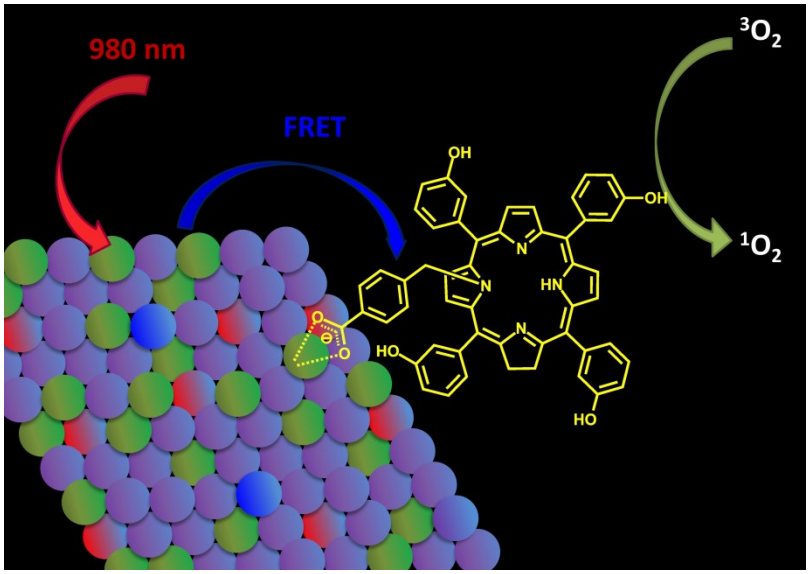

Figure 6.1 Schematic illustration of the nanoconstruct synthesized from $LiYF_4$:Tm^{3+}/Yb^{3+} nanoparticles and photosensitizer m-THPC-MBA(III). The diamond represents the surface of the nanoparticle: purple spheres = F^-, green spheres = Y^{3+}, red spheres = Yb^{3+}, and blue spheres = Tm^{3+}. The carboxylate from m-THPC-MBA(III) is coordinated to the Y^{3+} ions of the Ln^{3+}-UCNP *via* electrostatic interaction.

6.1 Transfer of Energy between Nanoparticles and Photosensitizers

The upconversion emission spectrum of $LiYF_4:Tm^{3+}/Yb^{3+}$-UCNPs and the UV/Vis absorption spectrum of m-THPC-MBA (III) are shown in Figure 6.2. There are two important conditions necessary for fluorescence resonant energy transfer (FRET) to occur between the UCNPs (donor) and the m-THPC-MBA (III) (acceptor): there must be overlap in the absorption (acceptor) and emission peaks (donor) shown in Figure 6.2 and the distance between the donor and acceptor should be shorter than 10 nm [78].

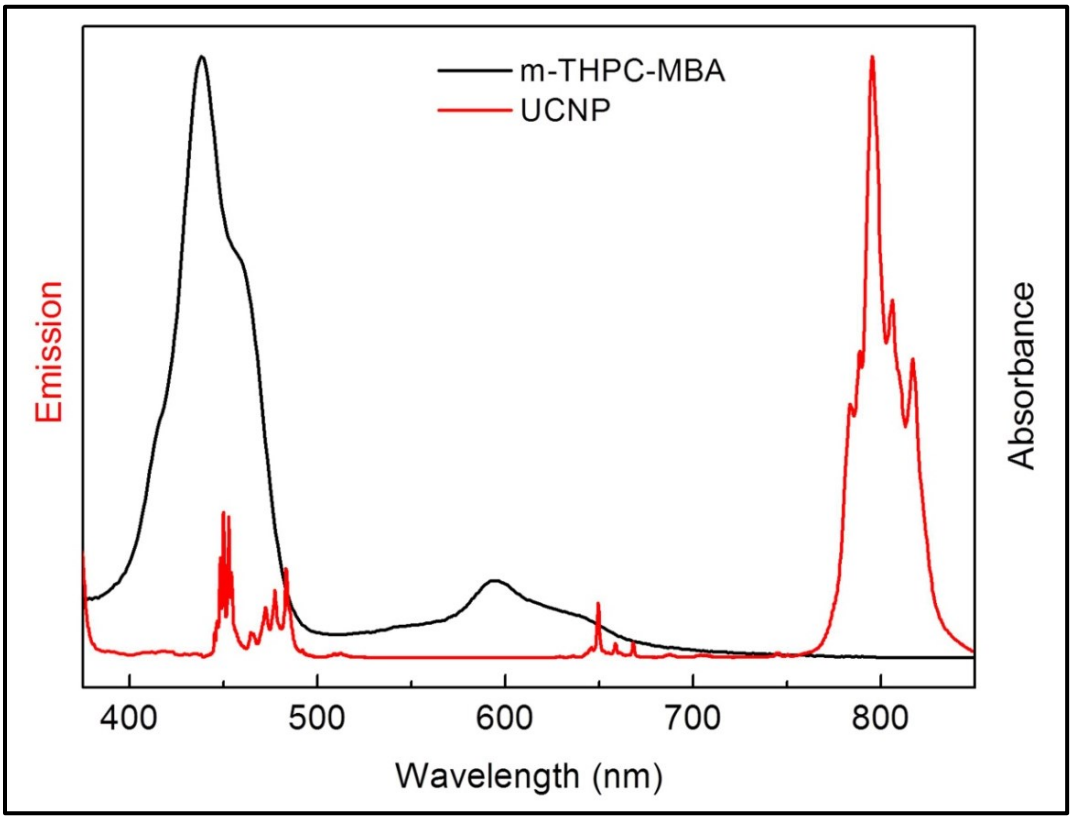

Figure 6.2. Overlap of (—) the absorption spectrum of m-THPC-MBA and (—) the luminescence emission spectrum of the $LiYF_4:Tm^{3+}/Yb^{3+}$-UCNPs. The energy transfer takes place in the blue region on the spectra.

The upconversion emission spectra of a dispersion of oleate-free $LiYF_4:Tm^{3+}/Yb^{3+}$-UCNPs (1wt% in ethanol/propylene glycol mixture) and a solution of m-THPC-MBA(III)-$LiYF_4:Tm^{3+}/Yb^{3+}$ are shown in Figure 6.3. We observe a decrease in the intensity of the blue peaks for the m-THPC-MBA(III)-$LiYF_4:Tm^{3+}/Yb^{3+}$-UCNPs in comparison to the respective peaks for the oleate-free $LiYF_4:Tm^{3+}/Yb^{3+}$-UCNPs.

The spectra were normalized with respect to the NIR emission peak at 800 nm and the ratio of the intensity of the blue emission bands for the solution of oleate-free-$LiYF_4:Tm^{3+}/Yb^{3+}$-UCNPs to m-THPC-MBA(III)-$LiYF_4:Tm^{3+}/Yb^{3+}$-UCNPs was found to be 3:2. This indicates that the binding of m-THPC-MBA on the UCNPs resulted in the quenching of the emission of the blue peaks, which clearly demonstrates that resonance energy transfer from the $LiYF_4:Tm^{3+}/Yb^{3+}$-UCNPs to the m-THPC-MBA(III) is occurring. The energy transfer efficiency was calculated using the following equation [79],

$$E = 1 - I_1/I_2 \qquad (14)$$

where E is the energy transfer efficiency, I_1 is the intensity of the m-THPC-MBA(III)- $LiYF_4:Tm^{3+}/Yb^{3+}$-UCNPs in the blue region, and I_2 is the intensity of the ligand-free $LiYF_4:Tm^{3+}/Yb^{3+}$-UCNPs at in the same region. The energy transfer efficiency was calculated to be ~33%. This result also confirms that the spatial separation, which was calculated to be 6.16 Å between the donor and the acceptor molecule is small enough to favor non-radiative energy transfer from the nanoparticle to the photosensitizer.

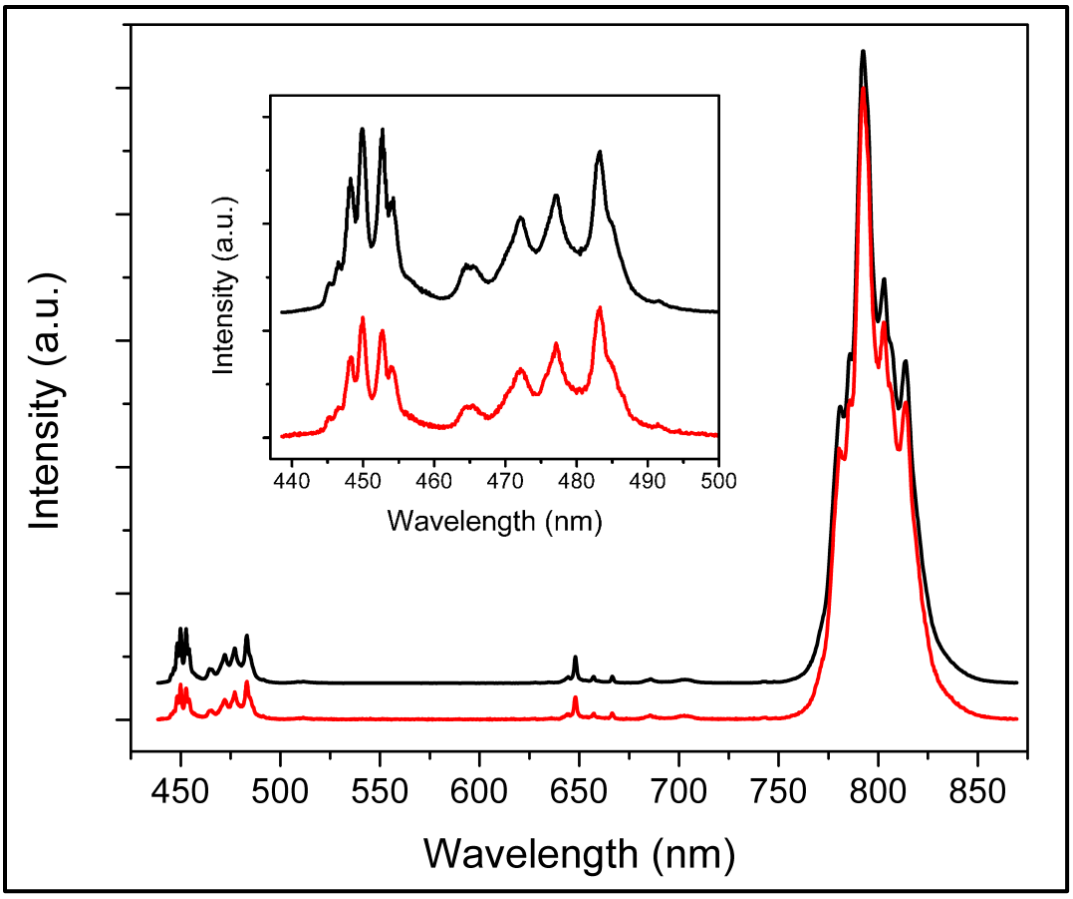

Figure 6.3. Upconverting emission spectra demonstrating the energy transfer between the Ln^{3+}-UCNPs and photosensitizer. A decrease of intensity was observed in the blue region when comparing the (—) oleate-free $LiYF_4$:Tm^{3+}/Yb^{3+}-UCNPs with (—) m-THPC-MBA(III)-$LiYF_4$:Tm^{3+}/Yb^{3+}-UCNPs.

6.2 Generation of Singlet Oxygen by m-THPC-MBA(III)

The generation of $^1O_2$ is primordial in photodynamic therapy, thus we initially assessed its production by the modified photosensitizer, m-THPC-MBA(III), under 435 nm (maximum absorption of m-THPC-MBA(III)) excitation (Figure 6.5) using the standard reaction of 1, 3-diphenylisobenzofuran (DPBF) with singlet oxygen. Figure 6.4 shows the absorption spectrum of DPBF and the cycloaddition reaction of singlet oxygen with the chemical trap. Upon cycloaddition with singlet oxygen, DPBF is known to form

an intermediate endoperoxode whose final degradation product no longer absorbs at 415 nm [67, 68]. A solution of DPBF (2.5 x 10^{-5} M) and m-THPC-MBA(III) (5 x 10^{-5} M) in propylene glycol/ethanol was exposed to a filtered light source of wavelength 435 nm over a period of 0 to 45 s at intervals of 5 s. Figure 6.5 shows the decrease in absorbance of DPBF at 415 nm as a function of radiation time. The absorbance of the trap reaches approximately zero after an irradiation time of 45 s, which demonstrates that the introduction of the electron donating group (MBA) as assessed by the generation of singlet oxygen.

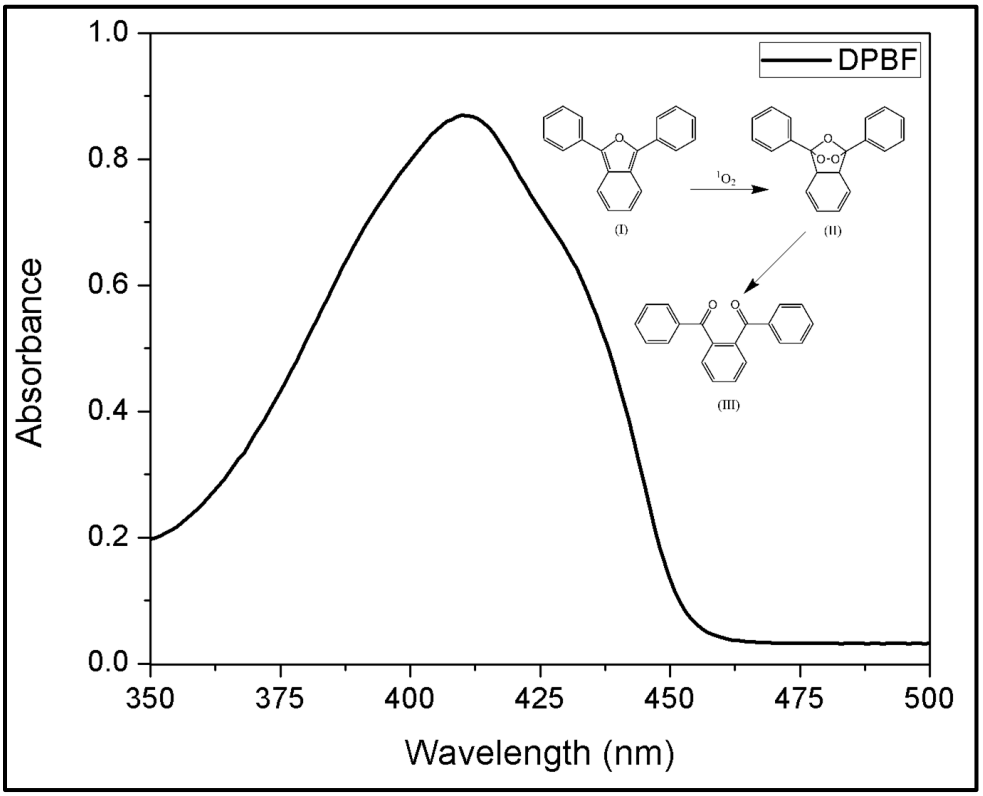

Figure 6.4. UV/Vis absorption spectrum of DPBF in ethanol/propylene glycol mixture solvent. Inset: 1,4-cycloaddition reaction between the singlet oxygen and DPBF that generate a colorless endoperoxide *o*-dibenzoylbenzene.

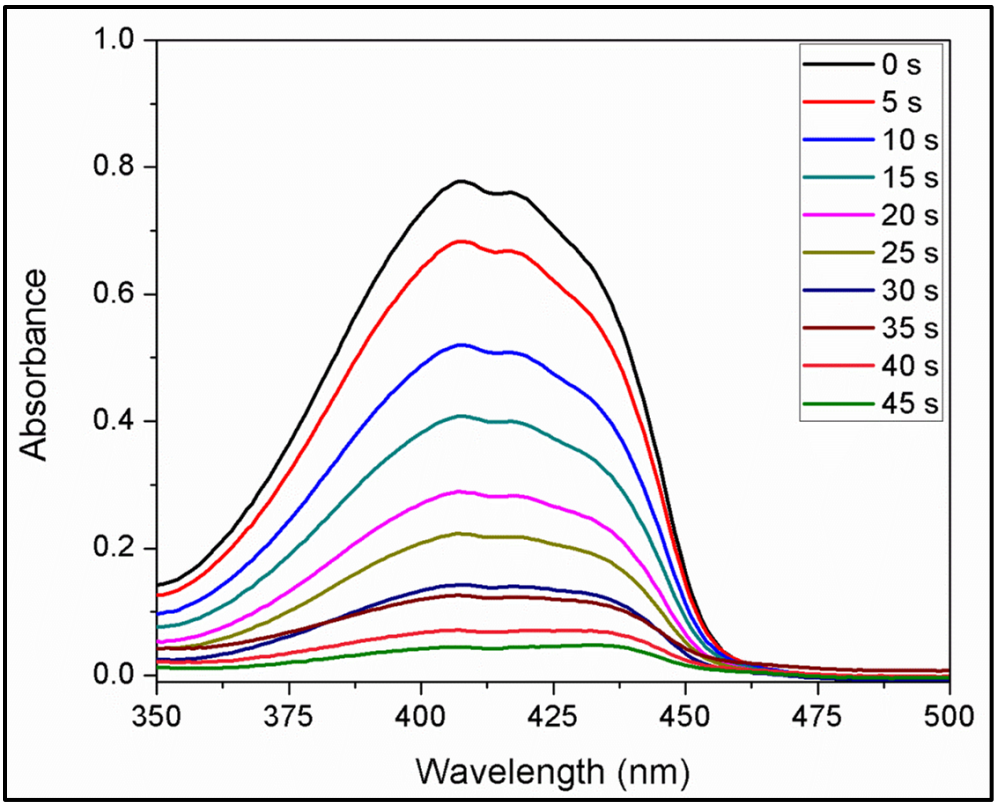

Figure 6.5. Decrease in the absorption of DPBF in a DPBF (2.5 x 10^{-5} M)/m-THPC-MBA (III) (5 x 10^{-5} M) solution as a function of irradiation time using 435 nm light.

6.3 Generation of Singlet Oxygen by the Nanoconstruct, m-THPC-MBA(III)-UCNP

The primary objective of this thesis was to investigate the functionalization of m-THPC to $LiYF_4$:Tm^{3+}/Yb^{3+}-UCNPs and to assess their potential to generate singlet oxygen under 980 nm excitation.

A 2 mL solution of DPBF (2.5 x 10^{-5} M) and m-THPC-MBA(III)-$LiYF_4$:Tm^{3+}/Yb^{3+}-UCNPs (1 mg/mL which correspond to 5 x 10^{-5} M) in an ethanol/propylene glycol mixture was exposed to an irradiation source of 980 nm over a period of 120 min at 10 minute intervals. Figure 6.6 shows the decrease in absorbance of DPBF at 415 nm as a function of irradiation time, which indicates that the amount of singlet oxygen production increases. The concentration of singlet oxygen generated was calculated from the

consumption of DPBF and it was found to be 2.11 x 10^{-5} M. The nanoconstruct has been shown to generate singlet oxygen for an irradiation time of 2 hours, which is the normal length for a PDT treatment, this suggests that the nanoconstruct could be a promising photosensitizer for the PDT.

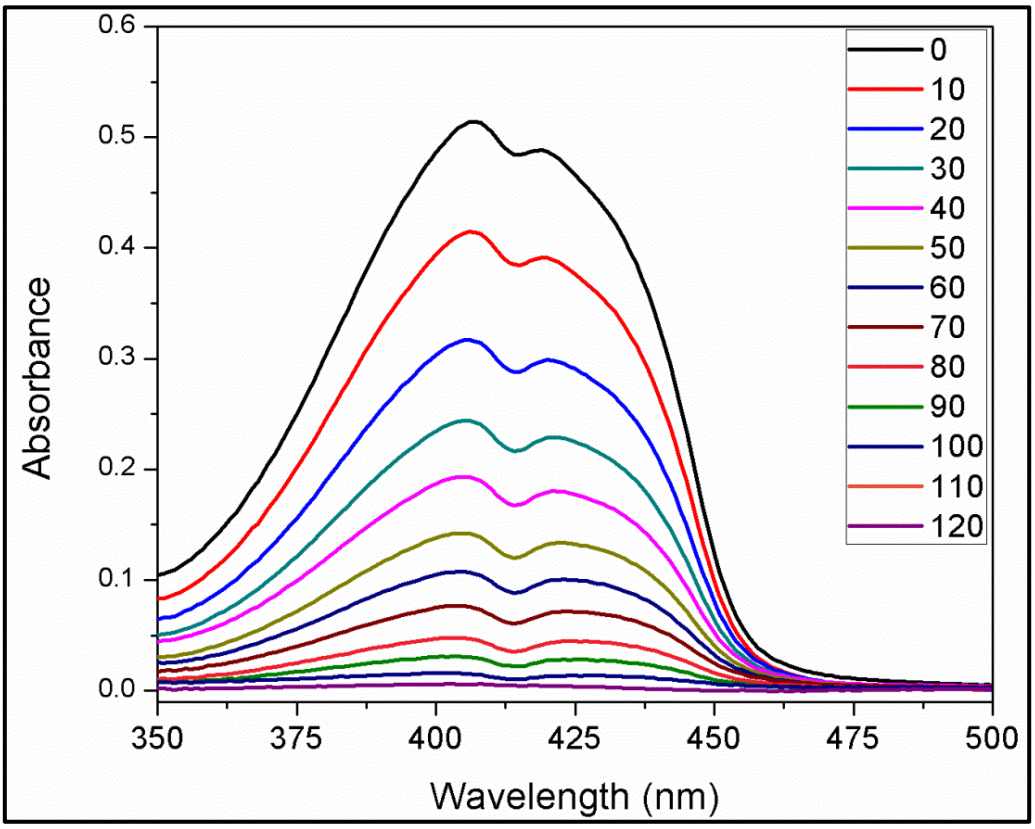

Figure 6.6. Decrease in the absorption of DPBF in a DPBF (2.5 x 10^{-5} M)/m-THPC-MBA-UCNPs (1 mg/mL) dispersion as a function of NIR irradiation time (min).

6.4 *In Vitro* Cell Viability Tests Showing the Applicability of Nanoconstruct in PDT *via* MTT Assay

The last part of our study the potential of the nanoconstruct as novel PDT agent was examined by studying *in vitro* cell viability in the absence and presence of irradiation at 980 nm. HeLa carcinoma cells were incubated for 4 hours with the nanoconstruct (m-

THPC-MBA(III)-$LiYF_4$:Tm^{3+}/Yb^{3+}-UCNPs) at concentrations of 0.004 to 0.1 mg/mL in PBS. Cell viability was assayed using the MTT assay, a method based on the activity of mitochondrial dehydrogenase [26]. The nanoconstruct demonstrated no intrinsic toxicity towards the cells when not irradiated as the cellular survival rate was identical to the control (Figure 6.7). The relative cell viability was obtained by comparing the survival rate of the sample that had been incubated with the nanoconstruct with cells that had not incubated with the nanoconstruct (the control sample). To assess the efficacy of the photodynamic effect, HeLa cells were incubated for 4 hours with the nanoconstruct at the same concentration as stated above, which represents a concentration of 0.10 to 2.50 μM of m-THPC-MBA(III) and irradiated for 1 hour using NIR radiation (980 nm). Cell death was observed from a minimum of 20% to a maximum of 70% in the concentration range 0.50 to 2.50 μM m-THPC-MBA (III) (Figure 6.7). Such a significant cell death demonstrates the possible applicability of the nanoconstructs in photodynamic therapy using NIR irradiation for the treatment in “deep” tissue

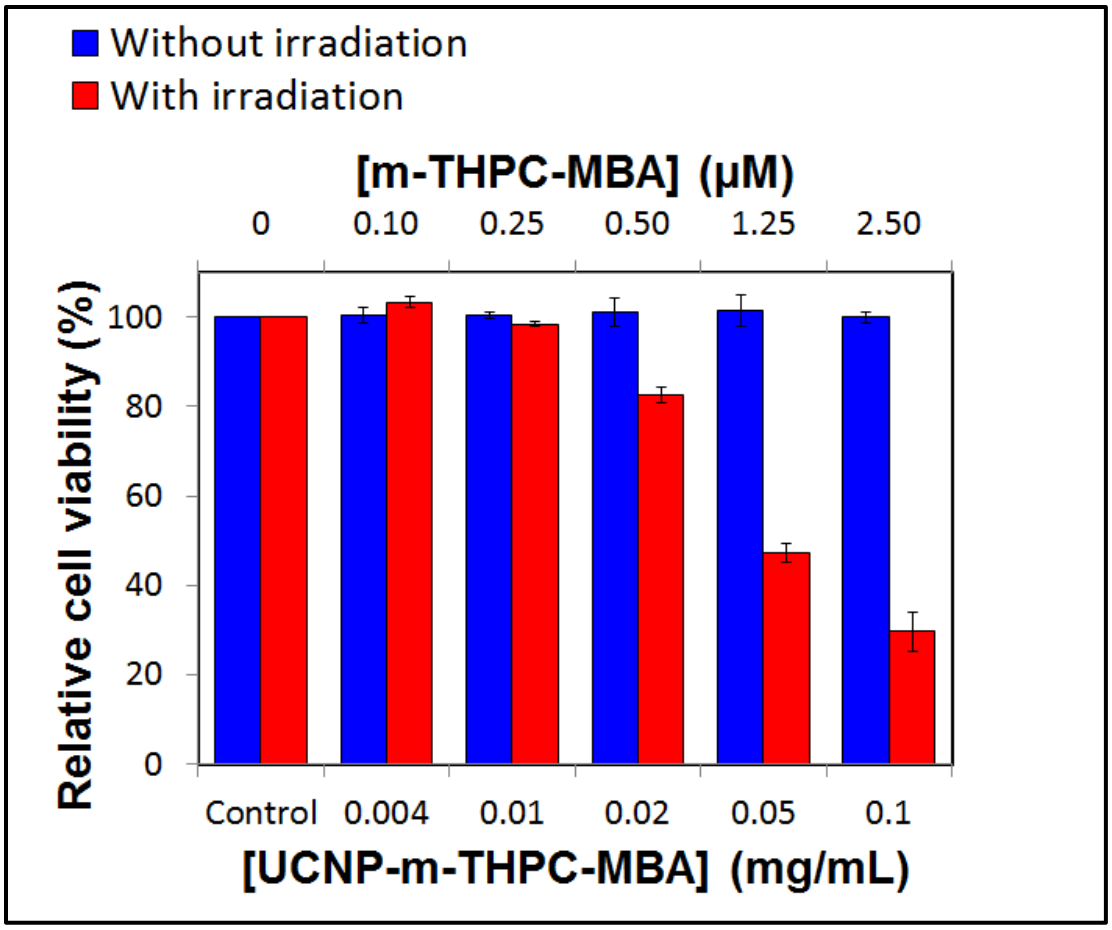

Figure 6.7. Viability of HeLa cancer cells following incubation with the m-THPC-MBA(III)-$LiYF_4$:Tm^{3+}/Yb^{3+}-UCNPs nanoconstructs and in the presence and absence of NIR irradiation (1 hour irradiation period). Bottom axis shows the concentration of the m-THPC-MBA(III)-$LiYF_4$:Tm^{3+}/Yb^{3+}-UCNPs construct while the top axis shows the equivalent concentration with respect to the PDT agent.

Chapter Seven - Conclusions

The photo-triggered treatment tool, photodynamic therapy can efficiently kill tumor cells by activating photosensitizers to generate reactive oxygen species $^1O_2$ under irradiation. However, conventional photodynamic therapy methods use visible or UV as the light source, which may achieve limited treatment efficacy on deep-seated tumors due to the low penetration depth. In view, of the advantages offered by nanoparticles, more specifically Ln^{3+} upconverting nanoparticles in this thesis we have addressed the challenge of utilizing the novel NIR-to-visible photodynamic therapy based on upconverting nanoparticles functionalized with a photosensitizer.

The thermal decomposition method was used to prepare the lanthanide-doped upconverting $LiYF_4:Tm^{3+}$ (0.5 mol%)/Yb^{3+} (25 mol%) nanoparticles. The synthesis successfully yields colloidal monodispersible nanoparticles with a diamond-like morphology, with an average size of 85 nm along the long diagonal with an aspect ratio of 1.7. These nanoparticles have a tetragonal crystal structure and show intense emission in the UV and visible region upon excitation with 980 nm light. The as-synthesized nanoparticles are hydrophobic therefore a surface modification was carried out to remove the hydrophobic ligand oleic acid, which not only result in aqueous dispersibility but also a positively charged surface that facilitates the conjugation of a negatively charged photosensitizers.

The second generation photosensitizer m-THPC with enhanced absorption of light at 652 nm does not make use of the optimal biological window in the 700-100 nm range. The approach employed in this work to make use of the optimal optical window differs significantly previous reports. The approach used in this work is based on modifying the

m-THPC using 4-(bromomethyl)benzoic acid (BMBA) to produce m-THPC-MBA(III) that permits the photosensitizer to be functionalized directly to the $LiYF_4:Tm^{3+}/Yb^{3+}$-UCNPs. In addition, this modification induces a bathochromic shift of the Soret band of the photosensitizer to obtain an excellent overlap with the blue emission peaks of the $LiYF_4:Tm^{3+}/Yb^{3+}$-UCNPs. The modification reaction of m-THPC produces three isomers which were isolated and characterized using LC-MS. Computational results allowed us to determine that the m-THPC-MBA(III) among the products isolated, which is responsible for the red shift of the Soret band from 417 nm to 438 nm, and ascertain that the linker is bonded to the nitrogen of the pyrrole ring.

The photosensitizer can be excited by irradiation of the $LiYF_4:Tm^{3+}/Yb^{3+}$-UCNPs at 980 nm to produce $^1O_2$. This demonstrates that the m-THPC-MBA molecules on the surface of the $LiYF_4:Tm^{3+}/Yb^{3+}$-UCNPs are excited *via* an energy transfer process and are capable of performing PDT. More importantly, using an irradiation wavelength of 980 nm would enable PDT in "deep" tissue. We also demonstrated that the nanoconstruct was capable of causing HeLa cell death up to 70% under 980 nm irradiation for a period of 1 hour. The general method reported can be applied to other drugs for the preparation of nanoparticles as drug carriers.

Chapter Eight - Future Work

Practical applications of UCNPs set demanding requirements on their optical properties, size and shape, surface chemistry, and clinical prospects, as well as their ability to incorporate a number of imaging and therapy modalities to achieve more accurate diagnostics and more effective therapeutics. In this chapter we would like to highlight future directions to be considered that could produce significant effects in the field.

The brightness of $LiYF_4:Tm^{3+}/Yb^{3+}$-UCNPs and in general of upconverting nanoparticles is still not at a satisfactory level especially at low power density of 10^{-2}-10^{-1} W/cm^2. The principle reason for this is the low quantum yield. Modification of the local environment around the lanthanide ions could be a promising avenue. However, the lanthanide ions possess low extinction coefficients, which is an intrinsic feature of f-f transitions. Therefore, coupling the UCNPs with quantum dots, plasmons, dyes or other doping ions with high absorption coefficients could provide an antenna effect similar to what has been used for lanthanide complexes to increase their efficiency.

The common excitation wavelength that is used is 980 nm. This wavelength overlaps with the absorption of water that may cause heating in biological tissues. Thus, shifting the wavelength to 800 nm would be an attractive option. The Nd^{3+} ion may be used for this purpose. $LiYF_4:Tm^{3+}/Yb^{3+}$-UCNPs have relatively large size of ~85 nm in the long diagonal and the sharp edges a result of their diamond morphology. This could inhibit their entry into cells. To maintain high emission efficiency and at the same time decrease their size, a core-shell structure should be used. The shell would protect the core thus minimizing surface related deactivation processes. A likely candidate is

$NaGdF_4:Tm^{3+}/Yb^{3+}$ as the core and $NaGdF_4:Nd^{3+}$ as the shell. In addition, it has been shown recently that the size and morphology (spherical, hexagonal) of $NaGdF_4$ may be using the thermal decomposition method.

The majority of available photosensitizer on the market are porphyrin derivatives that have a Soret band (high absorption coefficient) and relative weak Q-bands. The ideal photosensitizer for the synthesis of more efficient nanoconstruct such as the one proposed in this thesis require that the overlap between the Soret band and the emission of the UCNPs be maximized in order to obtain highly efficient energy transfer. In addition, photosensitizers should be synthesised which have higher absorption coefficient in the Soret band so that more efficient energy transfer may be achieved. Modification of m-THPC or other similar photosensitizers using an efficient electron donating group to shift the Soret band towards a lower wavelength would enable the use of the Tm^{3+} emission in the UV region which would result in more efficient energy transfer.

Using the platform developed multimodal UCNPs involving optical imaging, Magnetic Resonance Imaging (MRI), Positron Emission Tomography (PET), and X-ray Computed Tomography (CT) may be emerging as a new set of theranostic nanoprobes for a broad spectrum of biomedical applications.

References

1. R. L. Morris, K. Azizuddin, M. Lam, J. Berlin, A. Nieminen, M. E. Kenney, A. C. S. Samia, C. Burda and N. L. Oleinick, *Cancer Res.* 2003, **63**, 5194.

2. R. Bonnett, *Chem. Soc. Rev*. 1995, **24**, 19.

3. T. J. Dougherty, C. J. Gomer, B. W. Henderson, G. Jori, D. Kessel, M. Korbelik, J. Moan and Q. Peng, *J. Natl. Cancer Inst.,* 1998, **90**, 889.

4. T. J. Dougherty, *Photochem. Photobiol.,* 1993, **58**, 895.

5. J. C. M. Stewart, *Curr. Opin. Invest. Drugs,* 1993, **2**, 1279.

6. S. Mitra and T. H. Foster, *Photochem. Photobiol.,* 2005, **81**, 849.

7. A. Zimmermann, M. Ritsch-Marte and H. Kostron, *Photochem. Photobiol.,* 2001, **74**, 611.

8. M. O. Senge, *J. Photochem. Photobiol. B:Biol.,* 1992, **16**, 3.

9. R. Bonnett, R. D. White, U. –J. Winfield and M. C. Berenbaum, *Biochem. J.,* 1989, **261**, 277.

10. *Eur. Pat. Appl.* EP 337601 A1 19891018, 1989.

11. M. C. Berenbaum, S. L. Akande, R. Bonnett, H. Kaur, S. Ioannou, R. D. White and U. –J. Winfield, *Br. J. Cancer*, 1986, **54**, 717.

12. R. Bonnett, P. Charlesworth, B. D. Djelal, S. Foley, D. J. McGarvey and T. G. Truscott*, J. Chem. Soc., Perkin Trans.,* 1999, **2**, 325.

13. A. M. Smith, M. C. Mancini and S. Nie, *Nat. Nanotechnol*., 2009, **4**, 710.

14. G. M. Hale and M. R. Querry, *Appl. Opt.,* 1973, **12**, 555.

15. R. R. Allison, G. H. Downie, R Cuenca, X. Hu, C. J. H. Childs and C. H. Sibata. *Photodiagn Photodyn.,* 2004, **1**, 27.

16. Á. Juarranz, P. Jaén, F. Sanz-Rodríguez, J. Cuevas and S. González, *Clin. Transl. Oncol.,* 2008, **10**, 148.

17. F. Wang and X. Liu, *Chem. Soc. Rev.,* 2009, **38**, 976.

18. K. König, *J. Microsc.,* 2000, **200**, 83.

19. Y. I. Park, H. M. Kim, J. H. Kim, K. C. Moon, B. Yoo, K. T. Lee, N. Lee, Y. Choi, W. Park, D. Ling, K. Na, W. K. Moon, S. H. Choi, H. S. Park, S. Y. Yoon, Y. D. Suh, S. H. Lee and T. Hyeon, *Adv. Mater.,* 2012, **24**, 5755.

20. P. Zhang, W. Steelant, M. Kumar and M. Scholfield, *J. Am. Chem. Soc.,* 2007, **129**, 4526.

21. H. S. Qian, H. C. Guo, P. C.-L. Ho, R. Mahendran and Y. Zhang, *Small,* 2009, **5**, 2285.

22. B. Ungun, R. K. Prud'homme, S. J. Budijono, J. Shan, S. F. Lim, Y. Ju and R. Austin, *Opt. Express,* 2009, **17**, 80.

23. K. Liu, X. Liu, Q. Zeng, Y. Zhang, L. Tu, T. Liu, X. Kong, Y. Wang, F. Cao, S. A. G. Lambrechts, M. C. G. Aalders and H. Zhang, *ACS Nano,* 2012, **6**, 4054.

24. S. Cui, D. Yin, Y. Chen, Y. Di, H. Chen, Y. Ma, S. Achilefu and Y. Gu, *ACS Nano,* 2013, **7**, 676.

25. V. Mahalingam, F. Vetrone, R. Naccache, A. Speghini and J. A. Capobianco, *Adv. Funct. Mater.,* 2009, **21**, 4025.

26. M. V. Berridge and A. S. Tan, *Arch Biochem Biophys*., 1993, **303**, 474.

27. J. D. Spikes, *Primary Photo-Processes in Biology and Medicine,* R. V. Bensasson, G. Jori, E. J. Land and T. G.Truscott, Plenum Press, New York, 1985, pp. 209-227.

28. R. M. Szeimies, J. Dräger, C. Abels, M. Landthaler, *Photodynamic therapy and fluorescence diagnosis in dermatology*, P. Calzavara-Pinton, R. M. Szeimies, and B. Ortel, Elsevier Science, Amsterdam, 2001.

29. J. D. Spikes, *Photochem. Photobiol.,* 1997, **65S**, 142S.

30. B. W. Henderson and T. J. Dougherty, *Photochem. Photobiol*., 1992, **55,** 145.

31. T. J. Dougherty, C. J. Gomer, B. W. Henderson, G. Jori, D. Kessel, M. Korbelik, J. Moan and Q. Peng, *J. Natl. Cancer Inst.,* 1998, **90**, 889.

32. K. Lang, P. Kubat, J. Mosinger and D. M. Wagnerova, *J. Photochem. Photobiol. A*, 1998, **119,** 47.

33. F. Wilkinson, W. P. Helman, and A. B. Ross, *J. Phys. Ref. Data*, 1993, **22**, 113.

34. K. I. Salokhiddinov, I. M. Byteva, and G. P. Gurinovich, *J. Appl. Spectrosc.,* 1981, **34**, 561.

35. W. M. Sharman, C. M. Allen and J. E. van Lier, *Methods Enzymol*, 2000, **319**, 376.

36. C. S. Foote, *Photochem. Photobiol*., 1991, **54**, 659.

37. S. Cotton, *Lanthanide and Actinide Chemistry*, John Wiley & Sons, Ltd, Chichester, UK, 2006.

38. P. Atkins, T. Overton, J. Rourke, M. Weller, F. Armstrong, and M. Hagerman, *Inorganic Chemistry*, W. H. Freeman and Company, New York, 2010.

39. W. Koechner, and M. Bass, *Solid-State Lasers – A Graduate Text*, Springer–Verlag, New York, 2003.

40. H. G. Friedman, G. R. Choppin, and D. G. Feuerbacher*, J. Chem. Educ*., 1964, **41**, 354.

41. F. Auzel, *Chem. Rev.,* 2004, **104**, 139.

42. G. H. Dieke, *Spectra and energy levels of rare earth ions in crystals,* Interscience Publisher, New York, 1968.

43. R. Scheps, *Prog. Quant. Electr.,* 1996, **20**, 271.

44. F. Auzel, *C. R. Acad. Sci. (Paris)*, 1996, **262**, 1016.

45. F. Auzel, *C. R. Acad. Sci. (Paris)*, 1996, **263**, 819.

46. F. Auzel, *Proceedings of the IEEE,* 1973, **61**, 758.

47. N. Bloembergen, *Phys. Rev. Lett.,* 1959, **2**, 84.

48. J. G. Solé, L. E. Bausá, and D. Jaque, *An Introduction to the Optical Spectroscopy of Inorganic Solids*, John Wiley & Sons, Ltd, Hoboken, 2005.

49. S. Hüfner, *Optical Spectra of Transparent Rare Earth Compounds*, Academic Press, Inc., New York, 1978.

50. L. A. Riseberg, and H. W. Moos, *Phys. Rev*., 1968, **174,** 429.

51. F. Wang, Y. Han, C. S. Lim, Y. Lu, J. Wang, J. Xu, H. Chen, C. Zhang, M. Hong, and X. Liu, *Nature*, 2010, **463**, 1061.

52. H.-X. Mai, Y.-W. Zhang, R. Si, Z.-G. Yan, L.-d. Sun, L.-P. You, and C.-H. Yan, *J. Am. Chem. Soc.,* 2006, **128**, 6426.

53. A. Aebischer, S. Heer, D. Biner, K. Krämer, M. Haase, and H. U. Güdel, *Chem. Phys. Lett.,* 2005, **407**, 124.

54. J. Yin, Q. Zhang, T. Liu, X. Guo, M. Song, X. Wang and H. Zhang, *Nucl. Instr. Meth. Phys. Res. B*, 2009, **267**, 74.

55. J. B. Foresman, and AE. Frisch, *Exploring Chemistry with Electronic Structure Methods*, Gaussian, Inc., Pittsburgh, PA, 1996.

56. F. Jensen, *Introduction to Computational Chemistry*, John Wiley & Sons, Ltd, Chichester, UK, 2007.

57. E. S. E. Eriksson and L. A. Eriksson, *Phys. Chem. Chem. Phys.,* 2011, **13**, 7207.

58. R. E. Stratmann, G. E. Scuseria and M. J. Frisch, *J. Chem. Phys.,* 1998, **109**, 8218.

59. M. Gouterman, *J. Mol. Spectroscopy.,* 1961, **6**, 138.

60. M. Gouterman, *J. Chem. Phys.,* 1959, **30**, 1139.

61. D. Dolphin, *The Porphyrins*, Academic Press, Inc., New York, 1978.

62. M. Nappa and J. S. Valentine, *J. Am. Chem. Soc.,* 1978, **100**, 5075.

63. M. Rubio, B. O. Roos, L. Serrano-Andres, and M. Merchan, *J. Chem. Phys.,* 1999, **110**, 7202.

64. M. Y. R. Wang and B. M. Hoffman, *J. Am. Chem. Soc.,* 1984, **106**, 4235.

65. D. G. Whitten, I. G. Lopp, and P. D. Wildes, *J. Am. Chem. Soc.,* 1968, **90**, 7196.

66. N. Bodgan, F. Vetrone, G. Ozin and J. A. Capobianco, *Nano Lett.,* 2011, **11**, 835.

67. C. Hadjur, N. Lange, J. Rebstein, P. Monnier, H. Bergh and G.Wagnières, *J. Photochem. Photobiol. B: Biology,* 1998, **45**, 170.

68. W. Spiller, H. Kliesch, D. Wöhrele, S. Hackbarth, B. Röder and G. Schnurpfeil, *J. Porphyrins Phthalocyanines,* 1998, **2**, 145.

69. R. Bonnett, B. D. Djelal and A. Nguyen, *J. Porphyrins Phthalocyanines,* 2001, **5**, 652.

70. R. Bonnett, P. Charlesworth, B. D. Djelal, S. Foley, D. J. McGarvey and T. G. Truscott, *J. Chem. Soc., Perkin Trans.,* 1999, **2**, 325.

71. F. Würthner, T. E. Kaiser and C. R. Saha-Möller, *Angew. Chem. Int. Ed.,* 2011, **50**, 3376.

72. M. J. Frisch, G. W. Trucks, H. B. Schlegel, G. E. Scuseria, M. A. Robb, J. R. Cheeseman, G. Scalmani, V. Barone, B. Mennucci, G. A. Petersson, H. Nakatsuji, M. Cari-cato, X. Li, H. P. Hratchian, A. F. Izmaylov, J. Bloino, G. Zheng, J. L. Sonnenberg, M. Hada, M. Ehara, K. Toyota, R. Fukuda, J. Hasegawa, M. Ishida, T. Nakajima, Y. Honda, O. Kitao, H. Nakai, T. Vreven, J. A. Jr. Montgomery, J. E. Peralta, F. Ogliaro, M. Bearpark, J. J. Heyd, E. Brothers, K. N. Kudin, V. N. Staroverov, R. Kobayashi, J. Normand, K. Raghavachari, A. Rendell, J. C.Burant, S. S. Iyengar, J. Tomasi, M. Cossi, N. Rega, N. J. Millam, M. Klene, J. E. Knox,J. B. Cross, V. Bakken, C. Adamo,J. Jaramillo, R. Gomperts, R. E. Stratmann, O. Yazyev, A. J. Austin, R. Cammi, C. Pomelli, J. W. Ochterski, R. L. Martin, K. Morokuma, V. G. Zakrzewski, G. A. Voth, P. Salvador, J. J. Dannenberg, S. Dapprich, A. D. Daniels, Ö. Farkas, J. B. Foresman, J. V. Ortiz, J. Cioslowski and D. J. Fox, Gaussian 09, Revision **B.01**; Gaussian, Inc.; Wallingford, CT, 2009.

73. C. Lee, W. Yang and G. R. Parr, *Phys. Rev. B: Condens. Matter Mater. Phys.,* 1988, **37**, 785.

74. A. D. Becke, *J. Chem. Phys.,* 1993, **98**, 5648.

75. M. Cossi, N. Rega, G. Scalmani and V. Barone, *J. Comput. Chem.,* 2003, **24**, 669.

76. V. Barone and M. Cossi, *J. Phys. Chem. A.,* 1998, **102**, 1995.

77. E. S. E. Eriksson and L. A. Eriksson, *Phys. Chem. Chem. Phys.,* 2011, **13**, 11590.

78. P. Held, *An Introduction to Fluorescence Resonance Energy Transfer Technology and Its Application in Bioscience*, Bio Tek Instruments Inc., 2005.

79. A. R. Clapp, I. L. Medintz, J. M. Mauro, B. R. Fisher, M. G. Bawendi and H. Mattoussi, *J. Am. Chem. Soc.,* 2004, **126**, 301.